Title
On the physics-based processes behind production-induced seismicity in natural gas fields

Journal
Journal of Geophysical Research: Solid Earth, 122(5)

ISSN
2169-9313

Authors
Zbinden, Dominik
Rinaldi, Antonio Pio
Urpi, Luca
et al.

Publication Date
2017-05-01

DOI
10.1002/2017jb014003

Peer reviewed

AGU PUBLICATIONS

JGR

Journal of Geophysical Research: Solid Earth

RESEARCH ARTICLE
10.1002/2017JB014003

Key Points:
- Coupled hydromechanical modeling of production-induced seismicity
- Analysis of pore pressure and stress evolution on preexisting fault zone during natural gas production
- Multiphase fluid flow processes play a major role during natural gas extraction activities

Correspondence to:
D. Zbinden,
dominik.zbinden@sed.ethz.ch

Citation:
Zbinden, D., A. P. Rinaldi, L. Urpi, and S. Wiemer (2017), On the physics-based processes behind production-induced seismicity in natural gas fields, *J. Geophys. Res. Solid Earth*, *122*, 3792–3812, doi:10.1002/2017JB014003.

Received 18 JAN 2017
Accepted 23 APR 2017
Accepted article online 26 APR 2017
Published online 15 MAY 2017

On the physics-based processes behind production-induced seismicity in natural gas fields

Dominik Zbinden[1], Antonio Pio Rinaldi[1], Luca Urpi[1], and Stefan Wiemer[1]

[1]Swiss Seismological Service, Swiss Federal Institute of Technology, ETHZ, Zürich, Switzerland

Abstract Induced seismicity due to natural gas production is observed at different sites worldwide. Common understanding states that the pressure drop caused by gas production leads to compaction, which affects the stress field in the reservoir and the surrounding rock formations and hence reactivates preexisting faults and induces earthquakes. In this study, we show that the multiphase fluid flow involved in natural gas extraction activities should be included. We use a fully coupled fluid flow and geomechanics simulator, which accounts for stress-dependent permeability and linear poroelasticity, to better determine the conditions leading to fault reactivation. In our model setup, gas is produced from a porous reservoir, divided into two compartments that are offset by a normal fault. Results show that fluid flow plays a major role in pore pressure and stress evolution within the fault. Fault strength is significantly reduced due to fluid flow into the fault zone from the neighboring reservoir compartment and other formations. We also analyze scenarios for minimizing seismicity after a period of production, such as (i) well shut-in and (ii) gas reinjection. In the case of well shut-in, a highly stressed fault zone can still be reactivated several decades after production has ceased, although on average the shut-in results in a reduction in seismicity. In the case of gas reinjection, fault reactivation can be avoided if gas is injected directly into the compartment under depletion. However, gas reinjection into a neighboring compartment does not stop the fault from being reactivated.

1. Introduction

Anthropogenic activities related to energy production sometimes involve induced seismicity. Indeed, seismic events have been associated with artificial lakes used for hydropower, mining, geothermal power plants, oil and natural gas production, groundwater extraction, and wastewater disposal [*McGarr et al*., 2002; *Styles et al*., 2014]. The possible causes of induced seismicity can be grouped into two main categories: (i) the state of stress may vary in correlation with pressure changes caused by fluid injection or extraction, and (ii) the removal of physical support (e.g., mining) may affect the physical strength of the rock. The former is often considered the primary mechanism relating seismicity to oil and gas production, during which subsidence and compaction processes take place [*Ellsworth*, 2013; *Styles et al*., 2014].

In recent years, the seismicity rate, the economic impact, and the extent of public awareness and concern related to induced seismicity have greatly increased around the globe [e.g., *Ellsworth et al*., 2015; *Trutnevyte and Wiemer*, 2017; *Grigoli et al*., 2017]. Consequently, the number of scientific publications on the subject has also risen dramatically. Most studies, however, focus on injection-induced seismicity, showing that a complex relationship between pore pressure changes, poroelastic stress, and earthquakes is often at play during an induced earthquake sequence [*Shapiro and Dinske*, 2009; *Goertz-Allmann and Wiemer*, 2013; *Committee on Induced Seismicity Potential in Energy Technologies*, 2013; *Ellsworth*, 2013; *Rinaldi et al*., 2015b; *Chang and Segall*, 2016; *Catalli et al*., 2016; *Rutqvist et al*., 2016]. By contrast, seismicity during extraction operations has received little attention in the literature, and the relevant physical mechanisms underlying it are not as well understood.

Seismicity induced by the production of natural gas or oil has been observed in many sites worldwide in recent decades, and many more cases have gone unnoticed in remote or offshore locations with limited seismic monitoring. Several studies have indicated that the pressure drop in the gas reservoir caused by gas extraction may lead to reservoir compaction, thereby affecting the stress field in the surrounding rock formations. This can lead to ground surface subsidence and the reactivation of preexisting fault zones [e.g., *Grasso*, 1992; *Segall*, 1989]. In urban areas, induced earthquakes can cause damage to structures and pose a threat to the exposed population. Given the high public and economic impact, a detailed understanding of the physical processes that take place before a production-induced earthquake is crucial.

In Europe, several prominent locations exist where induced seismicity has been observed in the immediate vicinity of gas fields and related to gas production. In Rotenburg (northern Germany), a region with rather low seismic activity, a magnitude 4.4 earthquake occurred in 2004, and it was linked to the production taking place in a nearby gas field [*Dahm et al*., 2015]. In the Lacq gas field (southwestern France), the first induced earthquake occurred after the pressure in the reservoir had dropped by 30 MPa [*Bardainne et al*., 2008]. Over 2000 seismic events were observed between 1974 and 1997—with the largest having a magnitude of 4.2 [*Bardainne et al*., 2008]—and all interpretations of the evidence connect these earthquakes to the depletion of the gas reservoir [*Grasso and Wittlinger*, 1990].

Currently, the most prominent example of production-induced seismicity in natural gas fields is found in the Groningen gas field (the Netherlands), where seismicity has significantly increased over the last 25 years. The first event occurred after a pressure drop of 20 MPa in the reservoir [*TNO*, 2012]. Several seismic events of magnitude 3 or greater have been observed in the last 10 years, with the biggest recorded to date occurring in 2012 with a magnitude of 3.6 [*de Waal et al*., 2015; *van Thienen-Visser and Breunese*, 2015]. In 2014, given the increasing seismicity rate, the operators of the Groningen gas field decided to significantly lower the production rates [*van Thienen-Visser and Breunese*, 2015]. The gas field in Groningen is located in an urban area, and therefore controlling the subsidence and induced seismicity is an important issue from a public acceptance point of view. For this reason, subsidence and induced seismicity are both continuously monitored [e.g., *Hettema et al*., 2000, 2002; *TNO*, 2013] and numerically modeled [e.g., *Van Wees et al*., 2014; *Sanz et al*., 2015; *Wassing et al*., 2016; *Orlic*, 2016].

The three examples above show that induced seismicity due to gas production represents a concern for both industry and society. Research is therefore focusing on developing models to gain a better understanding of the hydraulic and geomechanical processes occurring during gas production. The simplest approach for modeling induced seismicity employs a calculation of Terzaghi's effective stress principle [*Terzaghi*, 1923] to evaluate failure on a fault zone neglecting the deformation of the medium [e.g., *Gischig and Wiemer*, 2013; *Rinaldi and Nespoli*, 2017]. Indeed, for injection studies, the increased pressure leads to a decrease of effective stress, hence shifting the Mohr-Coulomb criterion toward failure. However, the same approach cannot be applied in the case of production-induced seismicity; given a pressure decrease, the Mohr circles move to the right and the failure criterion is never reached, meaning that earthquakes can never be induced, in direct contradiction to field observations (Figure 1a).

The theory of linear poroelasticity [*Biot*, 1941] can explain the seismicity induced by pore pressure reduction. It has been shown that for an infinite, unbounded reservoir with no offset, the change of effective horizontal stress is proportional to the pressure change ΔP and can be described as $\Delta\sigma'_h = -\alpha(\nu/(1-\nu))\Delta P$, where α is the Biot-Willis coefficient and ν the Poisson's ratio. On the other hand, effective vertical stress changes as $\Delta\sigma'_v = -\alpha\Delta P$ [e.g., *Segall and Fitzgerald*, 1998; *Mulders*, 2003; *Wassing et al*., 2016; *Orlic*, 2016]. Given that ΔP is negative for fluid extraction, and assuming compressive stresses positive in an extensive stress regime (i.e., $\sigma'_v > \sigma'_h$), for a given Poisson's ratio, σ'_v changes more than σ'_h and, accordingly, the differential stress ($\sigma'_v - \sigma'_h$) increases for fluid extraction. Translating this into the Mohr diagram, the circles start to grow and the failure criterion can be reached (Figure 1b). However, evaluating the equations above using an initial effective normal stress of 20.7 MPa and an initial shear stress of 8.5 MPa, it can be seen that for a fault zone dipping 60° and for a reasonable pressure drop ($\Delta P > -40$ MPa), reactivation of the fault zone only occurs for low Poisson's ratio values ($\nu \leq 0.17$, Figure 1c). For a steeper fault (e.g., 80°), reactivation can no longer be achieved for $\nu \geq 0.17$ unless large pressure drops ($\Delta P \leq -95$ MPa) occur in the reservoir (Figure 1d). Since the Poisson's ratio ν is about 0.25 for most rocks [e.g., *Gercek*, 2007], an unbounded, infinite reservoir without an offset is clearly an oversimplified model that is not able to reproduce seismicity with large values of ν.

For this reason, a model with compartmentalized reservoirs and with a fault offset is needed to properly explain seismicity induced by gas production. The effect of a fault offset has already been analyzed in previous studies [e.g., *Mulders*, 2003; *van den Bogert*, 2015]. It has been shown that a fault offset enhances shear stress increase and that less of a pressure drop is needed to achieve fault reactivation [*van den Bogert*, 2015]. However, there are two major limitations present in the existing models:

1. Pore pressure is assumed to decrease simultaneously within the reservoir and intersecting fault zones, neglecting pressure gradients and multiphase fluid flow.
2. No fluid inflow occurs from the base rock and reservoir edges.

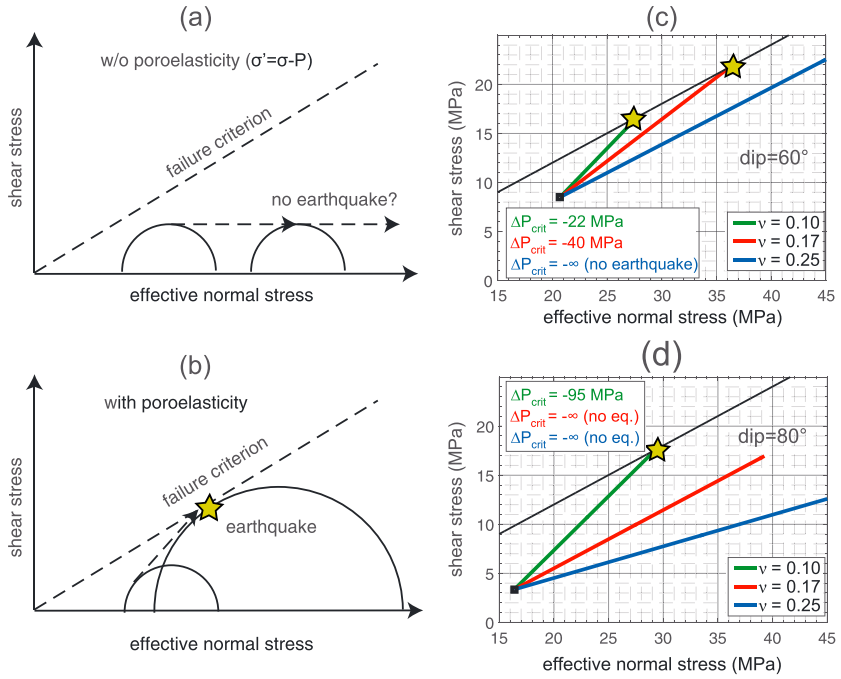

Figure 1. (a) Analysis of effective stress: For fluid extraction, pore pressure decreases in the reservoir and the effective stress increases accordingly. Hence, the Mohr circle moves to the right and no earthquake is induced. (b) Theory of linear poroelasticity: Because the horizontal effective stress increases less than the vertical effective stress, the Mohr circle grows and an earthquake can be induced. Approximation of an infinite, unbounded reservoir for fault dips of (c) 60° and (d) 80°. The required pressure drops to achieve reactivation are only realistic ($\Delta P \geq -40$ MPa) for an optimally oriented fault zone (i.e., 60°) and low Poisson's ratios. For a steep dipping fault (i.e., 80°) and an average Poisson's ratio for rocks (i.e., 0.25), the approximation fails to explain induced earthquakes. The initial effective normal stress and initial shear stress are 20.7 MPa and 8.5 MPa, respectively.

In this work, we show that fluid flow processes should not be neglected since they exert a strong influence on the evolution of pore pressure and stress within fault zones intersecting reservoirs.

We propose here a deterministic 2-D model using the TOUGH-FLAC simulator for modeling hydromechanical processes [*Rutqvist*, 2011]. This coupled fluid flow and geomechanics code has been frequently applied to the study of fault reactivation and seismicity induced by fluid injection, including the stimulation of enhanced geothermal systems [e.g., *Rutqvist et al*., 2013a; *Jeanne et al*., 2015; *Rinaldi et al*., 2015a] and carbon sequestration [e.g., *Cappa and Rutqvist*, 2011a; *Rinaldi and Rutqvist*, 2013; *Rinaldi et al*., 2015b, 2017; *Urpi et al*., 2016], as well as the hydraulic fracturing of shale gas reservoirs [*Rutqvist et al*., 2013b, 2015]. Applications of TOUGH-FLAC to gas production have so far been limited to studies on hydrate-bearing deposits and have not been applied to natural gas production from an aquifer [*Rutqvist et al*., 2009; *Rutqvist et al*., 2012]. The simulator is based on an explicit sequential approach in which the multicomponent and multiphase fluid flow solution is directly transferred to calculate the stress field in a geomechanical simulator. The updated stresses are then transferred back to the fluid flow simulator to account for stress-dependent permeability. Finally, if the stresses meet the conditions for failure, an "earthquake" is simulated by employing a strain-softening friction model to allow for a sudden slip in a preexisting fault zone. This enables us to calculate coseismic slip and rupture length, from which we can estimate the magnitude of the induced earthquake.

The objective of our study is to understand the evolution of stress and pressure in a compartmentalized gas reservoir and in an intersecting fault zone while it is producing gas at a constant rate. Furthermore, we aim at comparing the magnitude of the potential earthquakes that are induced. However, we do not aim at calibrating our model to a specific site. Hence, we use average hydraulic and mechanical properties for our model. In the first part of the paper, we show results from the simulation of different scenarios by varying production well setting, fault and caprock rheology, and production rates. We then analyze and compare the scenarios to achieve a broader understanding of the coupled hydromechanical processes occurring during the depletion

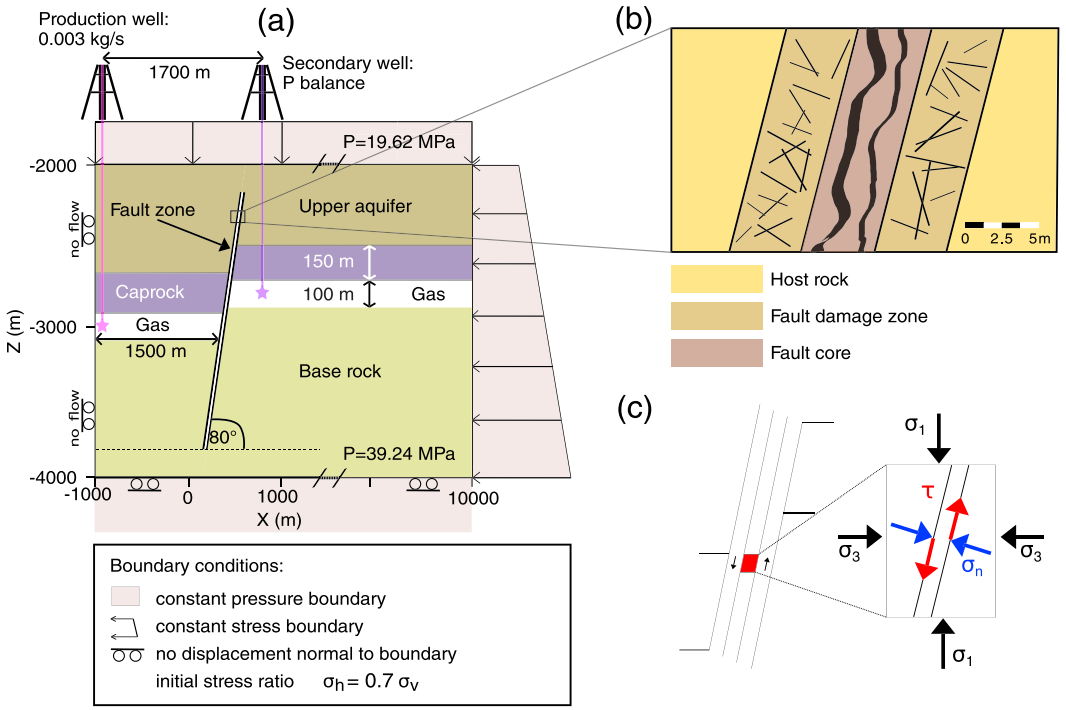

Figure 2. (a) Model with boundary conditions. In the multiple-well case, production in the secondary well is started in order to maintain similar pressure drops in both reservoir compartments. In the case of a plastically behaving caprock, the caprock has a thickness of 450 m. (b) Close-up view of the fault zone consisting of a highly fractured damage zone and a fault core with very low permeability. (c) Sketch of the stresses acting on a fault core element. Rupture is initiated when the shear stress τ equates the shear strength τ_s of the fault.

of a gas reservoir. Using the findings of the first part, we then propose scenarios to minimize seismicity and evaluate their effectiveness.

2. Model Setup

Our 2-D model consists of a 100 m thick semipervious gas reservoir located at a depth of 3000 m (where production occurs), which is a common depth for many gas reservoirs [*Bardainne et al.*, 2008; *Rahimpour-Bonab et al.*, 2010; *van Thienen-Visser and Breunese*, 2015]. The reservoir is underlain by low permeability base rock (down to a depth of 4000 m) and covered by 150 m thick brittle caprock (Figure 2a). The upper part of the model domain represents an overburden aquifer. The properties of the caprock and reservoir were chosen to be representative of a shale-rich caprock and a porous, weak sandstone reservoir, respectively. The reservoir is divided into two compartments by a normal fault (130 m offset). The low permeability fault zone serves as a seal for the left reservoir compartment and cuts the model domain from 2150 m to 3850 m depth. It can be reactivated if conditions for rupture are reached. We simulate different scenarios in order to investigate the response of the model in terms of stress and pressure evolution, rupture timing, and earthquake magnitude. For a base case scenario (scenario 1), we consider the two reservoir compartments to both be filled with gas and simulate production from the left compartment only at a production rate of 0.15 billion cubic meters per year (bcm/yr) for a 0.3 km^3 full-scale reservoir (i.e., thickness of 0.1 km, length of 3 km, and width of 1 km). This rate is downscaled to 75,000 m^3/yr for the 2-D simulation, in which we only account for one half of the reservoir's length (i.e., 1.5 km) due to reservoir symmetry, and in which the reservoir's width is only 1 m (2-D plane strain approximation). Using an air density of 1.225 kg m^{-3} at $T = 10$°C and $P = 0.1$ MPa, this results in a production rate of about 90,000 kg/yr, or 0.003 kg s^{-1}. For the other scenarios, we consider the following:

Scenario 2. It involves *multiple-well* configuration by adding a secondary well in the right reservoir compartment at a distance of 200 m from the fault zone. The production rate of the secondary well is set to experience a similar pressure drop in both reservoir compartments. This case aims at simulating a large gas

reservoir intersected by faults in which gas is produced from multiple wells separated by several kilometers [e.g., *Herber and De Jager*, 2010; *Van Hulten*, 2010].

Scenario 3. This scenario accounts for a *plastically behaving caprock* with a thickness of 450 m. The fault zone adjacent to this caprock is able to absorb much more plastic strain than brittle caprock. A prominent example of such a reservoir is the Groningen gas field, where the caprock consists of Zechstein salt [e.g., *Van Hulten*, 2010; *van Thienen-Visser and Breunese*, 2015].

Scenario 4. It considers *different production rates*, by doubling (0.31 bcm/yr, 0.006 kg s^{-1} for the 2-D approximation—scenario 4a) and dividing in half (0.077 bcm/yr, 0.0015 kg s^{-1} for the 2-D approximation —scenario 4b) the base case rate. The aim of simulating these scenarios is to test whether production rate changes have an effect on possible fault reactivation and the magnitude of the earthquake.

In addition to the scenarios listed above, we consider scenarios aimed at minimizing the occurrence of induced seismicity:

Scenario 5. This scenario is designated for *shut-in* of the production well after 40 (scenario 5a) and 50 years (scenario 5b).

Scenario 6. It involves *shut-in* of the production well after 50 years and a subsequent gas injection at a rate of 2.6 bcm/yr for a 0.3 km^3 full-scale reservoir (equivalent to 0.05 kg s^{-1} for the 2-D approximation) in the same well for 3 years (scenario 6a). In addition, we account for injection at the secondary well in the right compartment at 40 years until the end of the simulation while continuing production in the left compartment, either without production (scenario 6b) or with production (scenario 6c) on the right side for the first 40 years.

All the simulations are performed over a time period of 95 years, except for the low production rate case (scenario 4b), in which we double the simulation time to 190 years, and the shut-in case at 40 years (scenario 5a), in which we increase the simulation to 2000 years in order to investigate the long-term stress and pressure evolution both within and around the reservoir.

2.1. Numerical Modeling Approach and Setup

The numerical simulations are carried out using the coupled thermohydromechanical simulator TOUGH-FLAC [*Rutqvist et al.*, 2002; *Rutqvist*, 2011], which combines the multicomponent, multiphase, and heat transport software TOUGH2 [*Pruess et al.*, 2011] with the geomechanical simulator FLAC3D [*ITASCA*, 2013]. TOUGH2 solves the fluid flow and heat equations using the integral finite difference method in space and first-order implicit finite differences in time [*Pruess et al.*, 2011]. TOUGH2 can be run both isothermally or nonisothermally. For this study's simulations, we use isothermal conditions only. TOUGH2 allows for multicomponent, multiphase fluid flow and relative permeabilities for the different phases. The fluid components for the model can be chosen by different equations of state. For this study, we choose the module EOS3 that uses water and air—the latter representing the gas in our reservoir and the gas injected for the scenarios aimed at avoiding fault reactivation. The two components can be in a gaseous, liquid, or multiphase state depending on pressure and temperature.

The numerical model domain closely follows several studies relating to induced seismicity due to CO_2 sequestration [e.g., *Cappa and Rutqvist*, 2011a, 2011b, 2012; *Jeanne et al.*, 2014; *Mazzoldi et al.*, 2012; *Rinaldi et al.*, 2014a, 2014b, 2015b; *Rutqvist et al.*, 2014; *Urpi et al.*, 2016]. The 10 m wide fault zone consists of a fault core surrounded by a damage zone (Figure 2b). The fault core is modeled as solid 2.5 m wide elements having anisotropic elastoplastic properties. Ubiquitous joints are oriented as weak planes along the orientation of the fault, allowing the rupture to occur along the fault itself [*Cappa and Rutqvist*, 2011b]. The damage zone is an intensively fractured zone adjacent to the fault core and is modeled as a poroelastic medium where no slip is initiated. The fault core is usually significantly less permeable than the damage zone because it consists of highly deformed gouge, whereas the damage zone is intensively fractured and thus has a higher permeability [*Rinaldi et al.*, 2014a, 2014b, and references therein]. However, because of the gouge, the fault core is significantly weaker than the damage zone (i.e., resulting in greater deformation for the same applied stress). The fault zone intersects the multilayered model at an average distance of 1500 m from the production well. It dips toward the left reservoir compartment at an angle of 80°, and it has a length of about 1500 m. The length of the fault was chosen to avoid contact with the model boundary. The initial stresses acting on the fault are schematically shown in Figure 2c.

Table 1. Mechanical and Hydraulic Properties of the Rock Formations Used in the Numerical Model[a]

Layer	Upper Aquifer	Reservoir	Basal Aquifer	Caprock	Damage Zone	Fault Core
Young's modulus E (GPa)	40	20	40	40	40	10
Poisson's ratio ν (–)	0.25	0.25	0.25	0.25	0.25	0.25
Rock density ρ (kg/m^3)	2260	2260	2260	2260	2260	2260
Critical plastic strain[b]	-	-	-	-	-	10^{-5}
Peak friction angle θ (deg)	-	-	-	-	-	31
Residual friction angle θ (deg)	-	-	-	-	-	14
Dilation angle ψ (deg)	-	-	-	-	-	20
Porosity φ (%)	10	16	1	1	10	10
Permeability κ (m^2)	10^{-14}	10^{-13}	10^{-18}	10^{-21}	10^{-17}	10^{-19}
Residual gas saturation (–)	0.05	0.05	0.05	0.05	0.05	0.05
Residual liquid saturation (–)	0.3	0.3	0.3	0.3	0.3	0.3
van Genuchten [1980] ρ_0 (kPa)	19.9	19.9	621	621	19.9	19.9
van Genuchten [1980], m (–)	0.457	0.457	0.457	0.457	0.457	0.457

[a]Permeabilities in the reservoir and in the fault zone are stress dependent. The permeabilities indicated below are the initial values (initial stress conditions) [after *Cappa and Rutqvist*, 2011b; *Rinaldi et al.*, 2014a].
[b]Value is 0.2 for the case of a plastically behaving caprock (scenario 3).

Because of its high porosity, the reservoir is significantly weaker than the surrounding formations. We choose the elastic modulus of the reservoir to be 20 GPa, which is half the value of the caprock stiffness, which we assume to be nonfractured. The selection of these values is supported by laboratory measurements [*NAM*, 2013; *Hangx et al.*, 2010]. For the sake of simplicity, we set the stiffness of the base rock and upper aquifer to the stiffness of the caprock and assume a uniform Poisson's ratio of 0.25 and a uniform density of 2260 kg m^{-3} for all formations. The hydraulic and mechanical parameters of the different layers can be found in Table 1.

Figure 3a shows the initial stresses and pore pressure along the fault zone. The shear stress increases linearly with depth. The effective horizontal, vertical, and normal stresses increase almost linearly with depth. They deviate from linearity at the depth of the two reservoir compartments (where the pressure gradient is not hydrostatic) because the reservoir compartments are filled with gas (Figure 3b). The hydrostatic pressure gradient (9.81 MPa/km, 0.1 MPa at ground surface) is shown as a reference in Figure 3a. An initial linear temperature gradient going from 60°C at 2000 m depth to 110°C at 4000 m depth is applied and maintained over the entire simulation time. Hence, temperature and pressure at reservoir depth are 85°C and 29.53 MPa, respectively, so that air is in supercritical state. Since most components of natural gas are in a supercritical state in such conditions [*Nasrifar and Bolland*, 2006], air represents an appropriate choice for the gas phase in our model. As mentioned before, all the simulations are performed isothermally. This is justifiable because the largest flow velocities are expected to happen in the reservoir (i.e., the most permeable layer) and the vertical extent of the gas reservoir is rather small (230 m from the lower boundary of the left compartment to the

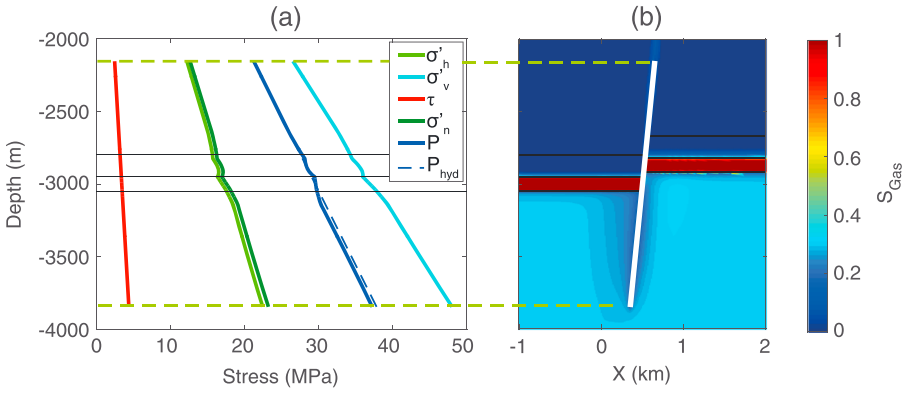

Figure 3. (a) Initial stress profiles along the fault zone. While the shear stress increases linearly with depth, the effective horizontal, vertical, and normal stresses slightly deviate from linearity due to nonhydrostatic conditions at the depth of the left and right gas reservoir compartments. (b) Initial gas saturation in the area around the fault zone. The horizontal black lines indicate the boundaries of the reservoir as well as the top of the caprock, whereas the white line in Figure 3b denotes the fault zone.

upper boundary of the right compartment). Hence, the difference in temperature from the lowest to the highest part of the reservoir is less than 6°C, meaning that temperature has a negligible influence on fluid flow and pressure distribution during the simulation. In all other formations that are connected to the reservoir, the permeabilities—and thus the flow velocities—are small, and the heat flow through convection plays a minor role. Induced thermoelastic stresses are in the order of a few percent of the expected poroelastic stresses and can be disregarded [*Segall and Fitzgerald*, 1998]. Because our model includes two components and two phases, we account for relative permeabilities by using *Corey*'s [1954] functions and for capillary pressure by applying *van Genuchten*'s [1980] approach.

In terms of geomechanical initial conditions, a normal faulting regime is assumed with a vertical stress σ_v initially corresponding to the maximum principal stress σ_1. The minimum horizontal stress σ_h is defined as 70% of σ_v, which is a near-critical value for a fault striking in the direction of the intermediate horizontal stress [*Cappa and Rutqvist*, 2011b; *Rinaldi et al*., 2014a]. The stress conditions at the top boundary are σ_v = 44.34 MPa, given by the weight of the overburden, and σ_h = 31.04 MPa. Both vertical and horizontal stresses increase linearly with depth by 22.17 MPa/km and 15.52 MPa/km, respectively.

Boundaries are open for fluid flow under the constraint of constant pore pressure except for the left boundary, where no-flow conditions are applied. Null normal displacement is imposed on the lower and left boundaries, while constant vertical stress is imposed on the top boundary and a horizontal stress that is linearly increasing in depth is imposed on the right boundary. The right boundary is set at nearly 10 km in order to minimize boundary effects (Figure 2a).

2.2. Stress-Dependent Permeability

Stress and pressure significantly affect the porosity (φ); therefore, they have a strong influence on permeability (κ) [*Rutqvist and Stephansson*, 2003]. In order to account for such effects, we apply a stress dependency on the permeability within the reservoir, the fault damage zone, and the fault core, which are presumably the domains most affected by stress and pressure changes. For a weakly fractured fault core and a highly fractured damage zone with joints randomly oriented, isotropic permeability changes can be assumed [*Rinaldi et al*., 2014a]. For materials with isotropic permeability, it is appropriate to allow the permeability to depend only on the mean effective stress σ'_M. For the fault zone, we thus use a modified version of a model introduced by *Davies and Davies* [2001] and later adjusted for reservoir rocks and fault zones by *Rutqvist and Tsang* [2002]:

$$\varphi = (\varphi_0 - \varphi_r)\exp\left(5\times10^{-8}\cdot\Delta\sigma'_M\right) + \varphi_r \tag{1}$$

$$\kappa = \kappa_0 \exp\left[22.2\left(\frac{\varphi}{\varphi_0} - 1\right)\right] \tag{2}$$

where φ_0 and φ_r are the initial and residual porosity, respectively, $\Delta\sigma'_M$ is the change of the mean effective stress in pascals, and κ_0 denotes the initial permeability. In the fault zone, φ_0 and φ_r are chosen to be 10 and 5%, respectively, to achieve permeability changes of about 1 order of magnitude during gas production.

For the reservoir rock, for which we set an initial porosity φ_0 = 16%, laboratory experiments have shown that permeability changes significantly less than 1 order of magnitude [*Schutjens et al*., 2001]. We apply a permeability law that is based on the modified Kozeny-Carman relationship, which is commonly used to model permeability changes in reservoir rocks [*Zoback*, 2010, and references therein]:

$$\kappa = \kappa_0\left(\frac{\varphi - \varphi_c}{\varphi_0 - \varphi_c}\right)^3\left(\frac{1 + \varphi_c - \varphi_0}{1 + \varphi_c - \varphi}\right)^2 \tag{3}$$

where φ_c is the percolation porosity, which is the limiting porosity at which the pores are disconnected and no longer contribute to flow. Note that φ in equation (3) is calculated from equation (1), in which we use a residual porosity φ_r = 14% for the reservoir rock. The percolation porosity is between 0 and 5% for most rocks [*Zoback*, 2010]. In our simulations, we always use φ_c = 0.1%.

2.3. Fault Slip, Seismic Moment, and Event Magnitude

The normal stress σ_n and shear stress τ acting on a plane are derived as

$$\begin{aligned}\sigma_n &= 0.5(\sigma_1 + \sigma_3) + 0.5(\sigma_1 - \sigma_3)\cos2\delta \\ \tau &= 0.5(\sigma_1 - \sigma_3)\sin2\delta\end{aligned} \tag{4}$$

where σ_1 is the maximum principal stress, σ_3 the minimum principal stress, and δ the angle between the fault plane and σ_3. Here we define compressive stresses to be positive. In our model, σ_1 and σ_3 are initially equal to the vertical stress σ_v and the minimum horizontal stress σ_h, respectively. In a porous medium, the behavior of the rock is controlled by the effective stress, which is the difference between the applied stress and the pore pressure [*Terzaghi*, 1923]:

$$\sigma_n^{'} = \sigma_n - P \tag{5}$$

where σ'_n is the effective normal stress and P the pore pressure. Note that pore pressure only affects the normal stress and not the shear stress. The production of gas leads to a pore pressure decrease within the reservoir and in neighboring formations and therefore yields an increase of σ'_n.

As described in section 2.1, the fault core is modeled as a ubiquitous joint fractured medium with weak planes oriented in the direction of the strike of the fault. Such weak planes are subjected to a Mohr-Coulomb criterion for shear failure

$$\tau_s = c + \mu_s \sigma_n^{'} \tag{6}$$

where τ_s is the shear strength (critical shear stress) of the fault above which the rupture is initiated, c the cohesion of the fault, and μ_s the static friction coefficient ($\mu_s = \tan(\theta)$, where θ is the angle of internal friction). The values of μ_s vary between 0.6 and 0.85 for most rocks [*Cappa and Rutqvist*, 2011b, and references therein]. In this study, we use $\mu_s = 0.6$ for all simulations. The friction evolves following a strain-softening behavior, allowing the simulation of a sudden slip on the fault. The friction coefficient depends on the plastic shear strain that accumulates if failure conditions are met. A dynamic friction coefficient $\mu_d = 0.25$ is reached for a plastic shear strain greater than a critical value of 10^{-5}. When simulating a plastically behaving caprock, such critical plastic shear strain is increased to 0.2 in the fault zone embedded within the caprock, thereby allowing for more plastic deformation rather than brittle rupture. The change of friction coefficient with plastic strain is equivalent to a slip-weakening model often applied in seismology and leads to a sudden slip when the Mohr-Coulomb failure criterion is reached. In all the simulations, we assumed a cohesionless fault (i.e., $c = 0$), which means that an earthquake is induced when $\tau/\sigma'_n = \mu_s$.

The earthquake moment magnitude, M_w, is estimated in two steps. First, we calculate the scalar seismic moment (M_0) from rupture geometry and fault strength. Using the ubiquitous joint model, we first estimate the average coseismic fault slip d_{avg} and the rupture length L. We then assume a circular rupture patch with diameter L extending in the direction of the strike of the fault to get the rupture area A. M_0 can then be written as [e.g., *Kanamori and Anderson*, 1975]

$$M_0 = GAd_{avg} \tag{7}$$

where G is the shear modulus of the fault core. In a second step, we use an empiric law to estimate the moment magnitude of the earthquake [e.g., *Kanamori and Brodsky*, 2004]:

$$M_w = \left(\frac{\log_{10} M_0}{1.5}\right) - 6.07 \tag{8}$$

where M_0 is given in Newton meter (N m). The model is able to distinguish between coseismic slip, which is accumulated during rupture (i.e., the earthquake), and aseismic deformation, which contributes to the total displacement along the fault but does not cause seismicity.

3. Results

We analyze the effect of different well configurations (i.e., single well versus multiple wells), caprock/fault rheology, and production rate on the stress evolution in the fault core. We compare each scenario to the results of a base case (single-well configuration) in terms of stress and pressure evolution within the fault zone. In order to investigate the effects of the different scenarios on the induced earthquake, we compare the slip along the fault and estimate the moment magnitude. Simulation results are summarized in Table 2.

3.1. Base Case (Scenario 1)

Figure 4a illustrates snapshots of the pressure decrease in the left reservoir compartment at four different points in time leading up to 50.8 years. The pressure in the reservoir decreases linearly with time by

Table 2. Time and Size of the Induced Earthquakes Simulated in This Study

Scenario	t (years)	d_{max} (cm)	d_{avg} (cm)	L (m)	M_0 (N m)	M_w
Base case	50.8	4.01	2.33	421	1.303e13	2.67
Multiple wells	54.3	5.88	3.46	226	5.545e12	2.43
Plastic caprock	51.2	3.25	2.03	213	2.907e12	2.24
Low production rate	101.0	4.30	2.48	447	1.555e13	2.72
High production rate	25.6	3.89	2.25	402	1.140e13	2.63

0.39 MPa/year. The base rock and the entire fault zone section near the producing reservoir are also affected by the pressure decline, while the right reservoir compartment and the relative near section of the fault zone are not visibly influenced. After about 50 years of production, the pressure has declined by 19.6 MPa, the fault zone is reactivated, and an earthquake is induced. The rupture point is located at a depth of 2955 m, near the intersection between the left reservoir compartment and the fault hanging wall. Figure 4b shows the stress evolution at this point. Starting from an initial state of effective normal stress σ'_n = 17.0 MPa and shear stress τ = 3.4 MPa, the stress path shows an almost linear increase of τ with σ'_n during the first years of production. However, after about 15 years of continuous production, the stress path bends toward higher shear stress, whereas the effective normal stress remains constant. After about 50 years, rupture occurs and the stress drops by 6.9 MPa to the value described by the residual friction (0.25 in our case). Figures 5a and 5b show the shear stress and shear strength before and after rupture, respectively. The shear stress changes in response to pore pressure decrease, and it reaches its highest value at the depth of the rupture point, whereas small changes are observed in the base rock (Figure 5a, red line). The shear strength is also affected by changes in pore pressure and total normal stress, resulting in an average increase of strength at depth of production (Figure 5a, blue line). Upon rupture, both shear stress and friction drop, defining the rupture length as the area of equal shear stress and strength (Figure 5b). Figure 5c shows the coseismic slip along the fault. The maximum slip (d_{max} = 4.01 cm) occurs at the rupture point, while the average slip (d_{avg}) and the rupture length of the earthquake are 2.33 cm and 421 m, respectively. The rupture propagates toward shallower depths through the caprock and further into the upper aquifer, while downward propagation stops at the intersection with the base rock, where the shear stress is at its minimum value. Hence, a significant portion of the slip is accumulated in the caprock and in the upper aquifer. Assuming a circular rupture, we calculate a scalar seismic moment of about $1.3 \cdot 10^{13}$ N m and a moment magnitude of M_w = 2.67 for the induced earthquake.

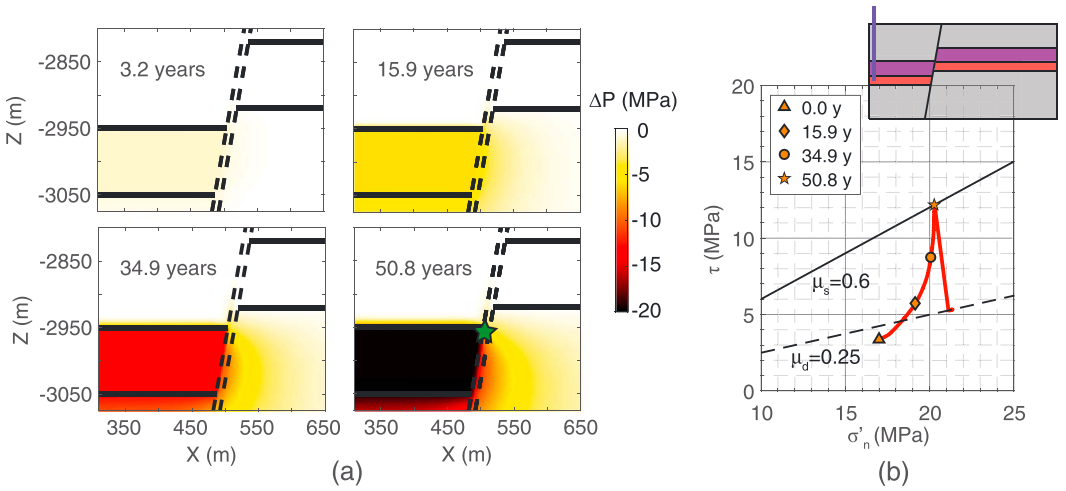

Figure 4. (a) Pressure evolution around the fault zone for the base case. The pressure in the left reservoir compartment drops consistently at 0.39 MPa/yr. The green star indicates the point of rupture at 2955 m depth after 50.8 years of production and a pressure decline of 19.6 MPa in the left compartment. (b) Stress evolution at the point of rupture for the base case. In the first few years, shear stress increases almost linearly with σ'_n. Subsequently, the stress path bends toward higher shear stress. Upon rupture ($\tau/\sigma'_n = \mu_s$), the shear stress is released and the friction drops to its dynamic value. At the top right, a sketch of the base case model is shown.

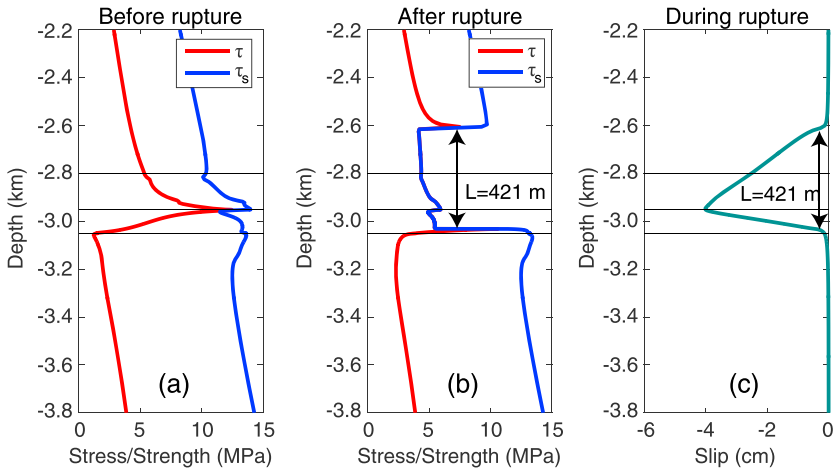

Figure 5. (a) Shear stress and strength along the fault core shortly before rupture is initiated. The highest shear stress is achieved at the intersection between the upper part of the left reservoir and the fault hanging wall. (b) Shear stress and strength immediately after rupture. The shear stress and strength coincide where coseismic slip has occurred. The rupture length is 421 m. (c) Coseismic slip along the fault (negative slip indicates downward displacement of the hanging wall). The maximum slip occurs at the rupture point (2955 m depth). A substantial part of the slip is accumulated in the caprock and the upper aquifer. The horizontal lines indicate the boundaries of the left reservoir compartment and its caprock.

3.2. Multiple Production Wells (Scenario 2)

Compared to the base case, in scenario 2 we include a secondary production well located in the right reservoir compartment. The production rate of the secondary well is chosen to maintain similar pressure drops in both reservoir compartments. A stress path comparison between the multiple-well case (scenario 2) and the single-well case (base case scenario) is shown in Figure 6a. The effective normal and shear stress increase much faster for the multiple-well scenario compared to the single-well case. Hence, the stress path hits the failure line at significantly higher stresses and the stress drop is considerably higher (10.0 MPa compared to 6.9 MPa). However, the timing of the induced earthquake (54.3 years) does not substantially differ from the base case. The simulated coseismic slip is shown in Figure 6b. Although the maximum slip and average slip are larger than the values obtained for the base case (d_{max} = 5.88 cm, d_{avg} = 3.46 cm), the rupture length is much smaller (L = 226 m). Similar to the base case, the downward rupture front stops at the lower part of the reservoir. However, the upward rupture front is halted at a depth of ~2820 m, close to the interface between the right reservoir compartment and its caprock. The estimated magnitude for the induced earthquake is M_w = 2.43, which is lower than in the single-well scenario despite the higher shear stress drop at the rupture point. The corresponding released seismic moment is less than half the seismic moment of the base case.

3.3. Plastically Behaving Caprock (Scenario 3)

In this section, we investigate the influence of fault and caprock rupture rheology (plastic instead of brittle) and the thickness of the caprock (450 m instead of 150 m) on stress evolution and induced seismicity. For the fault core above a depth of 2820 m, a larger critical plastic strain is defined to mimic the plastic behavior of the caprock. Figure 6c illustrates the stress path for the case of a plastic caprock in comparison to the base case. The stress paths look almost identical, and the ruptures occur at almost the same time. The small differences are due to the varying thickness of the caprock, which affects fluid flow and hence pressure and effective stress. Since plastic deformation only occurs after reaching the failure criterion, the change of caprock rheology (i.e., the larger critical plastic strain) does not have any influence on the processes that occur before rupture. On the other hand, it can be seen in Figure 6d that the plastically behaving caprock does have a strong influence on the slip along the fault. The maximum slip drops to 3.25 cm, the average slip to 2.03 cm, and the rupture length to 214 m, when compared to the base case. The slip significantly decreases when the rupture front reaches the plastically behaving caprock and rupture does not propagate through the caprock. The seismic moment for the scenario of a plastically behaving caprock is about $2.9 \cdot 10^{12}$ N m, which is less than one quarter of the seismic moment for the base case. The corresponding moment magnitude of the earthquake is M_w = 2.24.

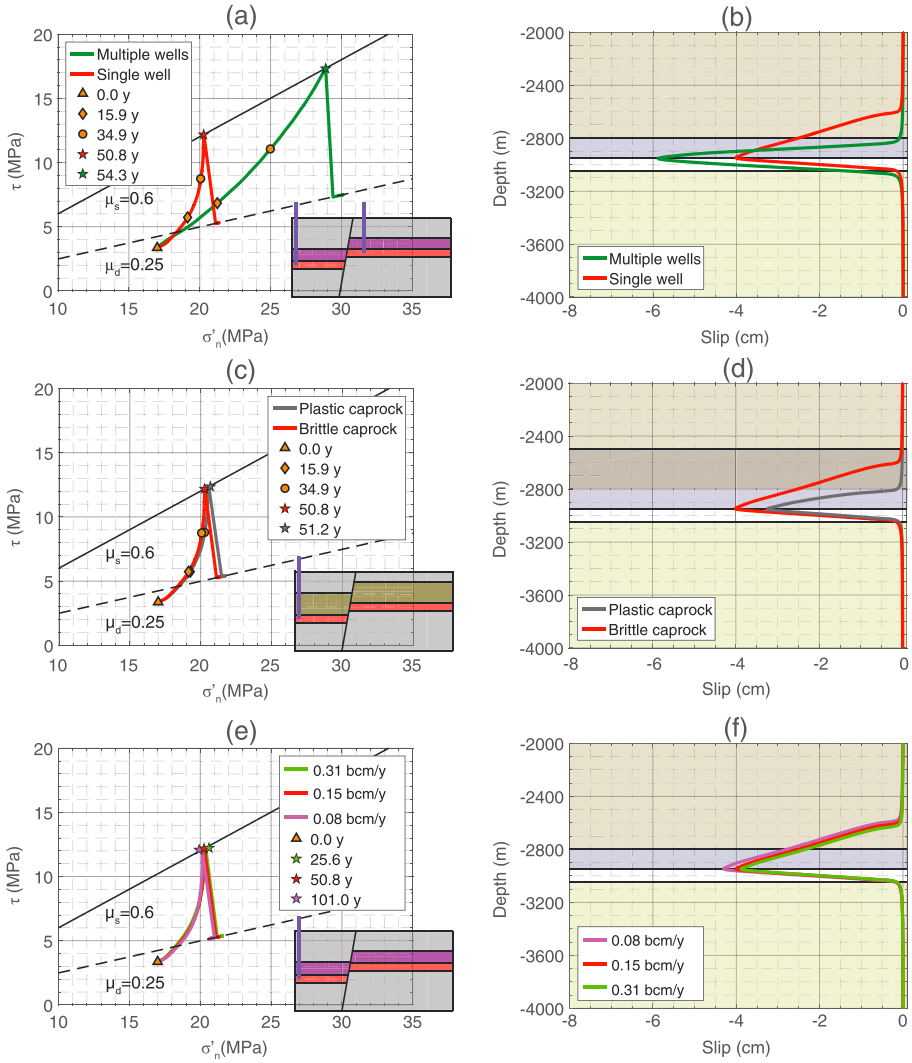

Figure 6. (a) Comparison of the stress paths of the multiple-well scenario (scenario 2) and the base case (single well). In the case of multiple production wells, the stress path moves toward much higher stresses, leading to a significantly higher shear stress drop at rupture. (b) Comparison of the fault slip between the multiple-well scenario (scenario 2) and the base case (single well). (c) Comparison of the stress paths in the case of a 450 m thick, plastically behaving caprock (scenario 3) and the base case (150 m thick, brittle caprock). The two stress paths look very similar. (d) Comparison of the fault slip between the case of a plastically behaving caprock (scenario 3) and the base case (brittle caprock). (e) Comparison of the stress paths for different production rates (scenarios 1, 4a, and 4b). The stress evolution is only weakly affected by the production rate. (f) Comparison of fault slip when using different production rates (scenarios 1, 4a, and 4b). (Figures 6a, 6c, and 6e) The stars indicate the stress state at rupture. Sketches of the different model configurations for each scenario are shown at the bottom right. (Figures 6b, 6d, and 6f) Negative slip indicates downward displacement of the hanging wall. The background colors indicate the different rock layers of the model to the left of the fault.

3.4. Production Rates (Scenario 4)

As a fourth scenario, we investigate the sensibility of the model to different production rates. We account for a production rate that is either doubled (i.e., 0.31 bcm/yr, 0.006 kg s^{-1} for the 2-D approximation) or halved (0.077 bcm/yr, 0.0015 kg s^{-1} for the 2-D approximation) with respect to the base case production rate. Figure 6e shows the stress paths for the two different cases under investigation and the base case. The trend for the stress changes is quite similar for all cases. For the high production rate, the stresses at rupture are slightly higher than they are for the base case, whereas for the low production rate, the stresses are slightly lower. The earthquake occurrence time is approximately inversely proportional to the production rate: it is longest for the smallest production rate (101.0 years) and shortest for the largest production rate (25.6 years). The fault slip is shown in Figure 6f. The coseismic slip is very similar for the three scenarios. The highest slip is

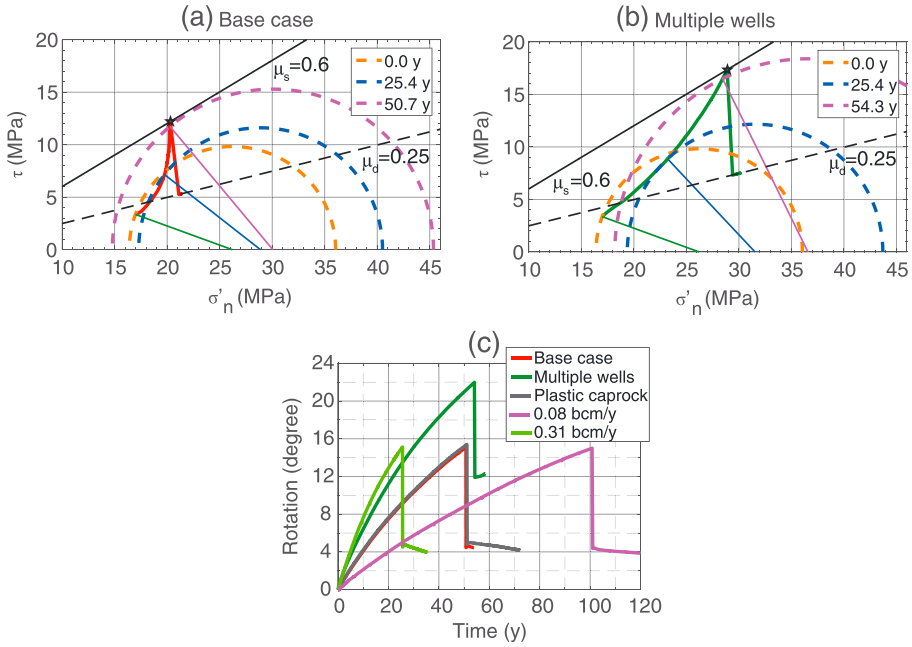

Figure 7. (a) Stress path of the base case and Mohr circles for the onset of production, at 25.4 years and at 50.7 years (shortly before rupture). (b) Stress path of the case of multiple wells (scenario 2) and Mohr circles for the onset of production, at 25.4 years and at 53.9 years (shortly before rupture). (c) Counterclockwise rotation of the principal stresses at the rupture point (in fault core at a depth of 2955 m) for scenarios 1, 2, 3, and 4. For the case of multiple wells (scenario 2), the principal stresses are rotated up to 22°, whereas for all other scenarios, the stresses are rotated by ~15°. The production rate has a strong influence on the reservoir compaction rate and hence on the rate of rotation.

achieved in the low production rate scenario (d_{max} = 4.30 cm, d_{avg} = 2.48 cm), while the lowest slip is obtained in the high production rate scenario (d_{max} = 3.89 cm, d_{avg} = 2.25 cm). The scalar seismic moments for the different production rate scenarios vary from $1.140 \cdot 10^{13}$ N m to $1.555 \cdot 10^{13}$ N m with corresponding magnitudes of 2.63 and 2.72, respectively.

4. Discussion

4.1. Stress Path

In this section, we discuss in detail the stress paths of the base case and the case of multiple wells (i.e., the two that sensibly differ from one another). Figure 7 shows the Mohr circles at the onset of production, at about 25 years, and shortly before failure at the rupture point (2955 m depth) for the base case and the multiple-well scenario (scenario 2). The line connecting the center of the Mohr circle to the corresponding point on the stress path is inclined at an angle of 2δ = 20° at the onset of production (Figures 7a and 7b, green line). This means that the angle between the fault and σ_1 is 10°. For the base case, considering the Mohr circle after about 25 years of production, the angle 2δ increases to 38°, meaning that the angle between the fault plane and σ_1 has increased to 19° (Figure 7a, blue line). Hence, the principal stresses at the rupture point have gone through a counterclockwise rotation of about 9° during the first 25 years of production. At the time of rupture (at 50.8 years for the base case), σ_1 and σ_3 have further rotated by 6°, leading to a total rotation of the principal stresses of about 15° when the earthquake is induced. At rupture, the stress axes are rotated back to 4.5° due to the shear stress drop and strain release. The stress rotation can be explained by the compaction of the left reservoir compartment. As the right reservoir compartment remains nearly undeformed for the base case, the compaction of the domain to the left of the fault yields a shear stress increase in the fault zone. In the case of multiple wells (scenario 2), both reservoir compartments undergo compaction. The rotation of the principal stresses is then even larger because the two compartments are offset by 130 m and more strain builds up in the fault segment between the two compartments (Figure 7b). All the analyzed scenarios with production from a confined reservoir present this feature (Figure 7c). In the case of a nonoffset and noncompartmentalized reservoir, pore pressure will

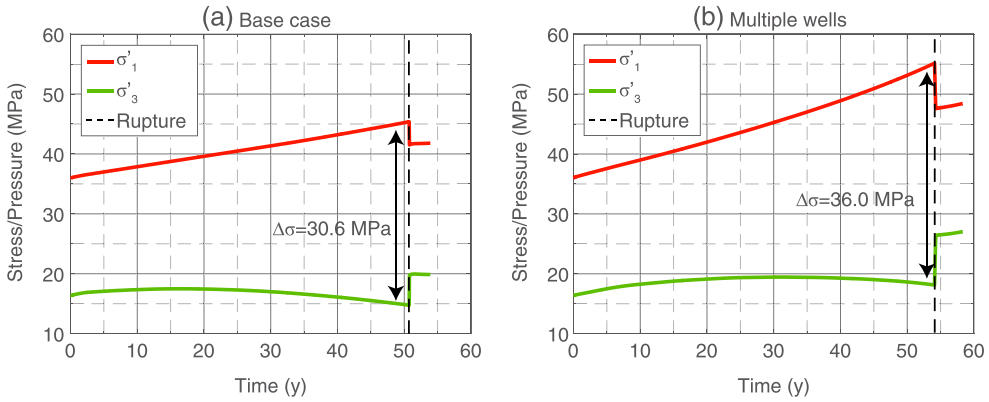

Figure 8. (a) Evolution of effective principal stresses at the rupture point (at a depth of 2955 m in the fault core) for the base case. The σ'_3 is reduced after ~15 years because of poroelastic effects occurring in the adjacent left reservoir compartment, whereas σ'_1 increases steadily. (b) Evolution of the effective principal stresses and pore pressure at the rupture point (at a depth of 2955 m in the fault core) for the multiple-well scenario (scenario 2). The increase in differential stress is more pronounced when compared to the base case.

follow a linear decrease, with consequent linear increases in shear stress and effective normal stress, leading still to the reactivation of a fault cutting through the reservoir [e.g., *Wassing et al.*, 2016; *Orlic*, 2016]. However, this only applies to less steep fault zones approaching the stringent conditions on Poisson's ratio and fault orientation discussed in Figure 1.

In theory, the rotation of the principal stress axes may lead to an increase in shear stress on a predetermined plane without necessarily increasing the differential stress ($\sigma'_1 - \sigma'_3$). However, as shown in Figures 7a and 7b, the gas production causes the Mohr circles to grow with time, with the centers of the circles shifting to higher effective normal stress. Figure 8 shows the evolution of σ'_1 and σ'_3 at the rupture point for the base case and the multiple-well case. For the base case (scenario 1), σ'_1 increases continuously with time (Figure 8a, red line), whereas σ'_3 first increases and then decreases to a value of 14.8 MPa at the end of the simulation (Figure 8a, green line). Thus, the differential stress, starting at a value of 19.6 MPa, increases during production and reaches about 30.6 MPa at time of rupture. In the case of multiple wells (scenario 2), both σ'_1 and σ'_3 reach higher values at the end of the simulation due to the larger pressure decrease in the fault zone, and the differential stress reaches a value of 36.0 MPa by the end of the simulation. The dissimilar evolution of σ'_1 and σ'_3 can be explained by the poroelastic effects taking place within the gas reservoir. For the base case, the linear increase in σ'_1 is strictly related to the weight of the overburden and to the pore pressure changes occurring within the left compartment of the production reservoir. However, the changes in the maximum principal stress (σ'_1) are not compensated for at the fault zone, leading to a relaxation (decrease) of the horizontal stress within the fault. Figure 8 indeed shows that during the initial phase, σ'_3 increases in reaction to the initial production phase. Then, when the pore pressure decrease shrinks, poroelastic effects start dominating and the horizontal stress decreases to counterbalance the vertical stress and strain changes within the fault zone, whose hanging wall deforms in the direction of the producing well. As a consequence, the differential stress increases. This evolution of stress is common to all the scenarios, with the magnitude of rotation depending on the case analyzed. For the multiple-well case (scenario 2), the increase of differential stress is more pronounced because the reservoir compartments are compacted at different depths, and both the fault hanging and foot wall are deformed in the direction of the respective producing well (in the left and right compartments, respectively).

In the base case scenario (scenario 1), the pressure at the well decreases almost linearly, whereas a nonlinear trend is observed within the fault zone (Figure 9a). At the fault, during the initial production phase, the pore pressure decreases at a rate similar to that of the entire left reservoir compartment. However, the rate of change decreases as production continues, up to an almost constant pressure evolution at time of rupture. The reason for this is that some gas is drawn from the right reservoir compartment into the fault zone due to the strong pressure gradient between the compartments. Indeed, Figure 9b shows the fluid flow after 25.4 years in and around the fault zone for the base case. The fault serves in the base case as a channel for the gas to flow from one compartment to the other, despite the rather low permeability of the fault. The

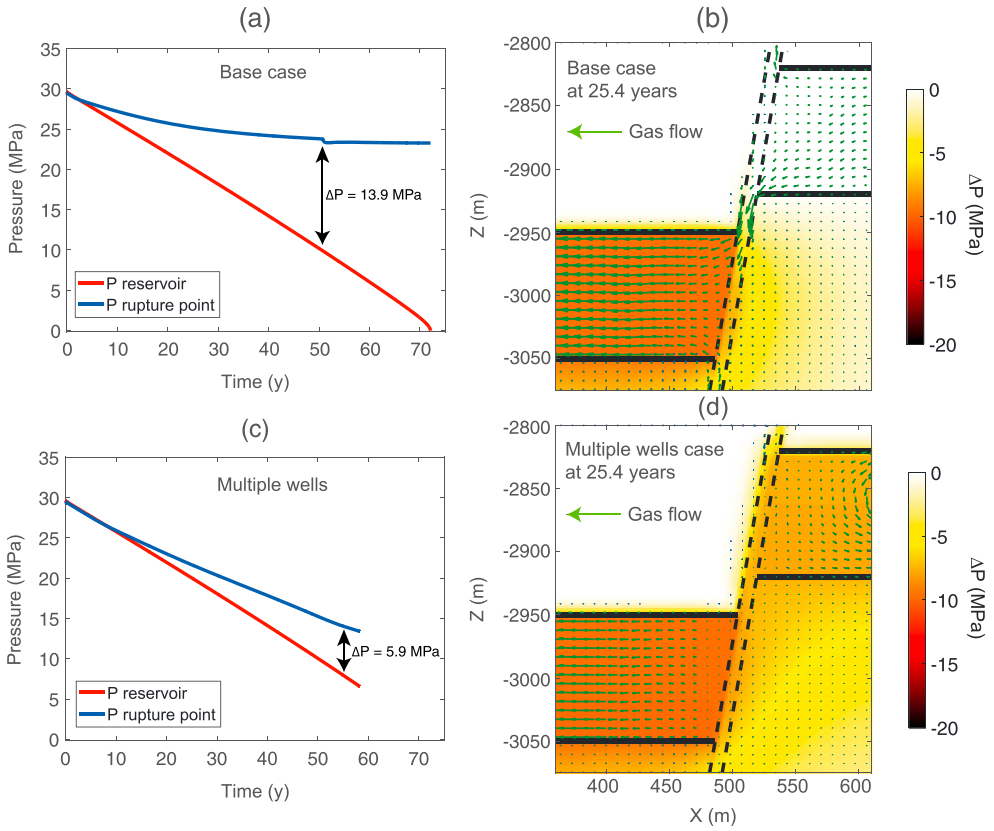

Figure 9. (a) Pore pressure evolution at the rupture point within the fault core (2955 m depth) and at the production well for the base case. At the time of rupture (50.8 years), the pressure difference between the rupture point and reservoir is 13.9 MPa. (b) Gas flow after 25.4 years of production around the fault zone in the base case. Gas inflow from the right compartment causes the pore pressure in the fault zone to decrease less than in the left reservoir compartment. (c) Pore pressure evolution at the rupture point within the fault core and in the production well in the case of multiple wells (scenario 2). At the time of rupture (54.3 years), the pressure difference between the rupture point and reservoir is 5.9 MPa. (d) Gas flow after 25.4 years of production around the fault zone in the multiple-well case (scenario 2). Gas flow is directed from the fault zone toward the two reservoir compartments; the pressure decrease in the fault zone is, however, still less than in the two reservoir compartments.

pore pressure evolution in the fault core does not influence the shear stress but directly affects the principal stresses, leading to a stable σ'_n and explaining the bending of the stress path.

In the case of multiple wells (scenario 2—Figure 9c), given production on both sides of the fault, the pressure decrease within the fault zone follows that of the left reservoir compartment, although a $\Delta P = 5.9$ MPa is still observed at time of rupture. Fluid flows from the fault zone toward either the left or the right reservoir compartment (Figure 9d). Consequently, σ'_n increases steadily, leading to a significantly larger stress drop at the time of rupture. The remaining and still significant difference in pore pressure between reservoir and fault zone is caused by fluid inflow from the edge of the reservoir (i.e., from the base rock). Hence, it is important to account for fluid flow even in a multiple-well case.

To summarize, the stress paths show a rotation of the principal stresses and an increase in differential stress in the fault zone. The stress rotation within the fault zone can be explained by the poroelastic compaction of the reservoir, which also leads to an increase in shear stress. The increase in differential stress can be explained by poroelastic effects, leading to less variation of σ'_3 compared to σ'_1, which increases continuously. A strong drop in pore pressure at the rupture point due to fluid outflow, as observed in the case of multiple wells (scenario 2), leads to larger stresses at failure when compared to the base case.

Extrapolating the concept to a population of faults in a 3-D model with different initial conditions (in terms of size, orientation, and strength), our results would lead to an accelerating seismicity with time given the

nonlinear response of the stress. Models neglecting fluid flow and reservoir offset could not predict such a strong shear stress increase. Since seismicity has indeed increased exponentially at some sites [e.g., *van Thienen-Visser and Breunese*, 2015], we consider our modeling results in this respect to be realistic.

4.2. Induced Earthquakes

For all simulations with continuous production carried out in this study, stress and pressure conditions resulted in the reactivation of a fault zone, although this may have depended on choices of mechanical and hydraulic parameters, as well as on the permeability dependence on stresses. Table 2 indicates the timing, the rupture geometry, and the size of the simulated induced events. All the simulations with a production rate of 0.15 bcm/yr (scenarios 1, 2, and 3) require about 50 years to reach a critical condition for fault reactivation, while the maximum (101.0 years) and minimum (25.6 years) times for reactivation were achieved by the low (0.077 bcm/yr) and high (0.31 bcm/yr) production rate scenarios (scenario 4), respectively. The time required to induce failure on a fault zone is well in agreement with the timing of seismicity observed at large producing gas fields [e.g., *de Waal et al*., 2015; *van Thienen-Visser and Breunese*, 2015; *Van Wees et al*., 2014]. The largest slip was achieved in the multiple-well scenario (scenario 2) followed by the base case (scenario 1), the low production case (scenario 4b), and the high production case (scenario 4a) that all resulted in a similar fault slip. The smallest slip was achieved for the case of a plastically behaving caprock (scenario 3). If we compare the simulated rupture area, results show that the multiple-well scenario (scenario 2) and the case of a plastically behaving caprock (scenario 3) have a significantly smaller rupture patch than the other scenarios, with the rupture front in this case stopping at a depth of ~2820 m. In the case of multiple-well production (scenario 2), at the top of the right reservoir compartment, the induced stress is oriented in the opposite direction of the tectonic stress, leading to a zone of low shear stress [*van den Bogert*, 2015]. Thus, the fault core above the right reservoir compartment (> -2820 m) is not critically stressed and requires higher stress variation before reaching failure conditions. The resulting scalar seismic moment and magnitude is therefore smaller for the multiple-well case ($M_w = 2.43$) compared to the base case ($M_w = 2.67$). Rupture in all scenarios mainly propagates upward—the resulting magnitude is therefore strongly influenced by the overlying material. Indeed, the smallest earthquake is generated in the case of a plastically behaving caprock (scenario 3) in which we estimate a moment magnitude of 2.24. In this case, the material can absorb much more plastic strain, thereby leading to a lower seismic moment and magnitude. We use the term "plastically behaving caprock", since we want to emphasize the plastic behavior of the fault zone at the depth of the caprock. We do not model the caprock as a plastic material, and thus we decided to avoid the description of the caprock as a viscoelastic material, which would have been a more accurate description for a salt caprock. The production rate only has a large impact on the time of reactivation, while very small differences are found in the resulting failure slip and magnitude. The high production rate (scenario 4a) results in an earthquake of $M_w = 2.63$, whereas for the low production rate (scenario 4b), the resulting moment magnitude is $M_w = 2.72$.

4.3. Mitigation Scenarios

Given the findings of the previous sections, we investigate different scenarios aimed at minimizing seismicity. In the first part, we analyze the effect of well shut-in after 40 (scenario 5a) and 50 years (scenario 5b) of production (i.e., shortly before fault reactivation). In these two scenarios, we consider production from the left reservoir only prior to shut-in. In the second part, we consider production and subsequent gas injection. The first injection case accounts for gas injected in the left compartment after 50 years of production (scenario 6a). The second injection case accounts for 40 years of production in the left reservoir only and a subsequent injection in the right reservoir continuing production in the left compartment (scenario 6b). Finally, in the third injection case, both the left and right compartments are under production for 40 years, then injection occurs in the right reservoir compartment while continuing production in the left compartment (scenario 6c).

Figure 10a shows the stress paths for the case of production shut-in after 40 years and 50 years of production (scenario 5) in comparison to the base case. Right after shut-in, in both scenarios the effective normal stress decreases, whereas the shear stress slightly increases, i.e., the condition moves toward failure. As pressure stabilizes in the reservoir, in the scenario of shut-in at 40 years (scenario 5a), the stress path changes direction and moves toward the initial stress state; however, in the case of well shut-in at 50 years (scenario 5b), the state of stress state at the fault zone is already too close to failure; hence, reactivation occurs despite ceasing production. Note that about 40 years elapse from the time of shut-in (50 years) to the time of fault reactivation

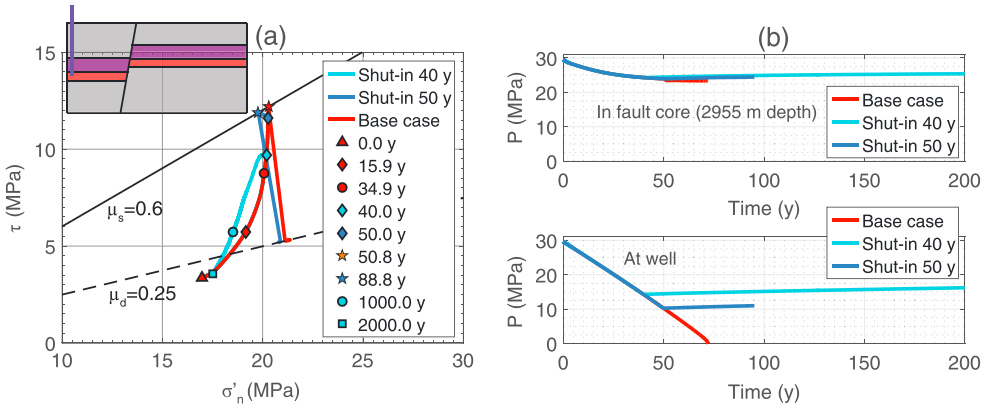

Figure 10. (a) Stress paths in the fault core at 2955 m depth in the case of well shut-in in the left compartment after 40 and 50 years in comparison to the base case. In the case of shut-in at 40 years (scenario 5a), the stresses in the fault relax and approach the stress state prior to production. For shut-in at 50 years (scenario 5b), the fault is so close to failure that it is reactivated despite ceasing production. (b) Pore pressure evolution in the fault core at 2955 m depth and at the well in the shut-in scenarios (scenarios 5a and 5b). After shut-in, the pressure increase in the fault zone due to gas inflow from the right compartment leads to a reduction in effective normal stress in the fault zone, whereas the pressure increase in the reservoir leads to expansion and a decrease in shear stress in the fault zone. The model configuration for the shut-in scenarios is illustrated at the top left of Figure 10a.

(88.8 years). Hence, if faults are in a critical state due to production, an induced earthquake is possible even several decades after production shut-in. Extrapolating again to a diverse population of faults, our model would predict that the complete shut-in of gas production would lead to an average decrease in seismicity, but not to total seismic quiescence, because faults in very critical stress states could still be reactivated. Hence, this could predict very long "aftershock" sequences after production has been terminated.

The key mechanism behind the stress change is the evolution of the pore pressure at the fault zone (Figure 10b). In the case of well shut-in at 40 years (scenario 5a), the pressure within the fault and at the well slowly increases with time after production halts. This pressure increase can be explained as being related to the gas inflow from the right compartment, given the large pressure gradient between the two compartments. As a direct, rapid effect, the pressure increase leads to a reduction in the fault's normal effective stress. However, a slower process is also involved: the pressure increases in the entire left compartment, leading to its expansion, and as a result, the shear stress in the fault zone decreases. The effect is visible in the case of shut-in after 40 years (scenario 5a), and about 2000 years must pass before returning to the state of stress prior to production. For the case of shut-in after 50 years of production (scenario 5b), the relaxation of the left compartment takes place after the fault has been reactivated.

We also investigate three scenarios involving gas reinjection. Here we reinject the same gas that is being produced (i.e., air). In the case of reinjection in the same producing compartment (scenario 6a), a rapid reservoir expansion occurs, and the shear stress decreases immediately, thereby stabilizing the fault (Figure 11a). Subsequently, as the pressure increases, effective normal stress decreases and the stress state approaches the state of stress prior to production. It takes about 3 years to return to the initial stress condition. In this scenario, the amount of gas produced and injected is exactly the same (0.15 bcm/yr over 50 years equals 2.5 bcm/yr over 3 years). While a shut-in after 50 years results in an induced event after some decades (scenario 5b), an injection right after shut-in stabilizes the fault (scenario 6a). However, gas reinjection can also lead to even more critical conditions if it occurs in the wrong compartment. Indeed, when gas injection occurs only in the right reservoir compartment, an earthquake is always induced, regardless of the production occurring in that compartment (scenarios 6b and 6c—Figure 11a). The stress paths first move away from the failure line; this is related to a decrease in shear stress because of the expansion of the right reservoir compartment. However, the gas inflow into the fault is augmented by the greater pressure in the right compartment, which leads, after some time delay (~1.5 years), to an increased pore pressure within the fault (Figure 11b) and thus to a decrease in its effective normal stress. For both scenarios where gas is injected in the right compartment (scenarios 6b and 6c), an earthquake is induced. For scenario 6b, reactivation occurs 6 years after the start of the injection operation, whereas 8 years is needed for scenario 6c.

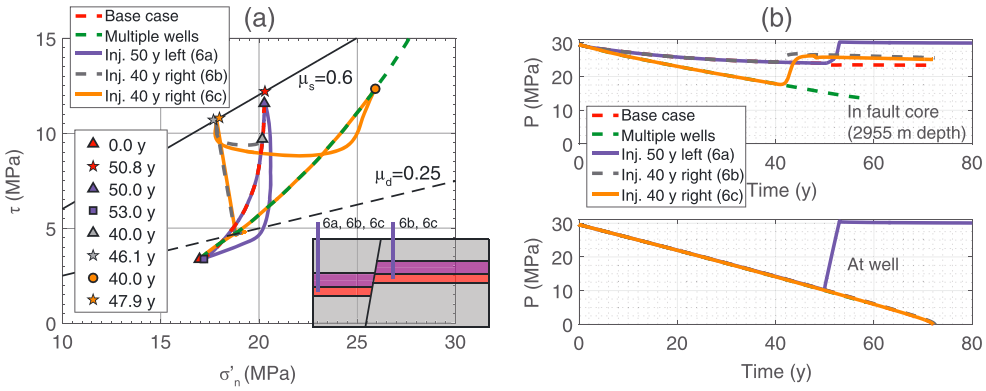

Figure 11. (a) Stress paths in the fault core at 2955 m depth in the case of gas injection in the left compartment after 50 years of production (scenario 6a) or in the right compartment while continuing production in the left compartment, either without (scenario 6b) or with (scenario 6c) production in the right compartment prior to injection. In the case of injection in the left compartment (scenario 6a), the shear stress decreases immediately after the onset of injection and the fault is stabilized. In the cases of injection in the right compartment (scenarios 6b and 6c), the stress paths move to the left because of the pore pressure increase in the fault zone, and an earthquake is induced. (b) Pore pressure evolution in the fault core at 2955 m depth and at the well in the injection scenarios. After injection, the pressure in the fault core increases in all scenarios. However, the pressure in the left compartment is only visibly affected by the case of injecting directly into the left compartment (scenario 6a).

Note that the main contribution to fault destabilization in reinjection scenarios is not an increase in shear stress but a reduction in fault strength. Figure 12a shows the shear stress and strength profile along the fault for scenario 6b. The reduction in fault strength is caused by the gas inflow from the right reservoir compartment. This scenario is a prime example to illustrate the importance of fluid flow when simulating scenarios aimed at avoiding fault reactivation where both production and injection processes are involved. The fault slip for the mitigation scenarios where fault reactivation could not be avoided is shown in Figure 12b. In the case of shut-in at 50 years (scenario 5b), the fault slip is slightly larger when compared to the base case, mostly because the pore pressure in the fault zone is larger than average, thereby causing increased propagation of the rupture front. The moment magnitude of the event for the case of shut-in at 50 years is 2.77 compared to 2.67 for the base case. For the reinjection scenarios (scenarios 6b and 6c), a zone of large slip expands from the upper part of the left compartment (~2950 m depth) to the upper part of the right compartment (~2820 m depth). Because of the high pressure in the fault zone adjacent to the right compartment,

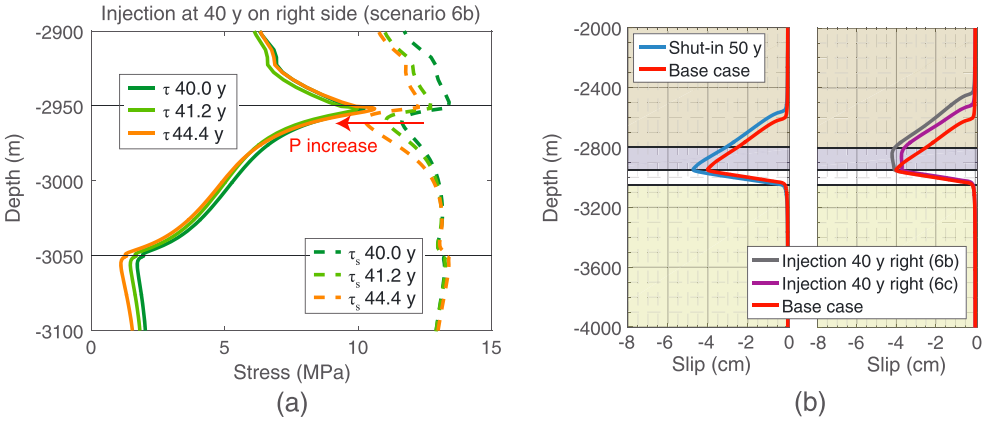

Figure 12. (a) Shear stress and strength profiles in the fault zone in the case of injection on the right side after 40 years (scenario 6b) for three distinct times after injection. The main portion of the destabilization of the fault is provided by a reduction in shear strength due to the pore pressure increase, whereas the shear stress does not change significantly. (b) Fault slip in the mitigation scenarios where fault reactivation could not be avoided (negative slip indicates downward displacement of the hanging wall). Injection into the right compartment (scenarios 6b and 6c) leads to gas inflow into the fault zone and to a decrease in fault strength. Thus, rupture propagates more easily, and the magnitudes of the induced events are higher.

the fault strength is reduced and rupture can easily propagate throughout this zone. This leads to a magnitude of 2.92 for scenario 6b, and a magnitude of 2.81 for scenario 6c. The magnitude of scenario 6b is slightly larger because the pressure in the fault is higher as a consequence of the absent production phase prior to injection.

Accounting for a population of faults and compartments, reinjection could then result in an average increase in seismicity if nearby compartments are in production and only a few of them are switched to reinjection. On the other hand, if wells were placed at relatively large distances to avoid production from neighboring compartments, the reinjection strategy would successfully reduce the seismic activity.

5. Conclusions

This study focuses on investigating the physical processes occurring on a bounding fault zone intersecting a gas reservoir during production activities. The proposed model allows for a much more accurate analysis of the stress and pressure evolution within the fault. We describe three processes affecting the stress path:

1. The compaction of the reservoir leads to rotation of the principal stresses, which in turn increases the shear stress in the fault zone.
2. The pressure drop in the gas reservoir strongly affects the horizontal and vertical stress acting on the fault through poroelastic effects, leading to an increase in differential stress and thus to an increase in shear stress.
3. Fluid flow into and out of the fault zone strongly affects the pore pressure evolution, hence altering the effective normal stress acting on the fault.

The observed fluid flow strongly depends on the chosen scenario. In all scenarios, the pressure drop in the producing reservoir compartment was significantly stronger than the pressure drop in the fault zone (i.e., at the rupture point). Hence, we conclude that the assumption of similar pressure drops in the fault and adjacent reservoirs, as suggested in previous studies [e.g., *Mulders*, 2003; *Orlic et al*., 2013; *van den Bogert*, 2015; *Wassing et al*., 2016; *Orlic*, 2016; *Juanes et al*., 2016], is a poor approximation of several physical processes. The deviation of the magnitudes in the different scenarios can be explained by different shear stress accumulation during production, different pore pressure distribution in the fault (i.e., fault strength), and different caprock rheology. A multiple-well scenario (scenario 2) has shown that the induced earthquake is smaller when the two compartments are depleted simultaneously (Figure 6b).

Our model was not designed to estimate a maximum magnitude for an induced earthquake during natural gas extraction. The magnitude estimations in this study can be used for comparing different scenarios, although the absolute values strongly depend on several model constants and assumptions: (i) the difference between peak and residual friction may be larger, leading to a larger average slip and rupture area; (ii) the rupture might propagate further into the third dimension (which we have not modeled here), leading to a substantially larger rupture area than the one assumed for a circular patch; (iii) the reservoir thickness may be larger, yielding both a larger rupture area and slip; and (iv) the fault stiffness might be significantly larger. For example, a fault with a stiffness of 20 GPa rupturing on a plane of 500 × 1500 m (where the latter number indicates the extension into the third dimension) with an average displacement of 5 cm would result in an induced earthquake with magnitude M_w = 3.6. This magnitude is well within the range of induced earthquakes recorded in the field at a reservoir depth similar to that used in our model [*van Thienen-Visser and Breunese*, 2015].

Concerning the timing of the fault reactivation, in most scenarios the earthquakes are induced after about 50 years and a pressure drop of ~20 MPa in the reservoir. However, different factors such as the fault permeability, fault offset, mechanical parameters of the rock layers, and the initial stress state exert strong influences on the timing. An overpressurized reservoir [e.g., *Segall et al*., 1994; *Wassing et al*., 2016, and references therein] yields lower effective normal stresses at the onset of production, and hence intersecting faults are closer to failure and less of a pressure drop is needed to achieve fault reactivation.

The results of simulations aimed at testing prevention strategies show that a fault zone does not reactivate if production shut-in occurs before some critical conditions are met. The results also suggest that reinjection in the producing reservoir compartment can reduce the chance of rupture even in a highly critically stressed fault, whereas injection in nearby compartments without stopping production at the primary reservoir may not be an effective strategy to prevent fault reactivation.

Although we obtain very reasonable results, our model has some limitations. Recent studies have shown that a proper 2-D approximation can provide a reliable solution when compared to a full 3-D model [*Rinaldi et al*., 2015b; *Rinaldi et al*., 2014c]. However, a full 3-D application may provide a better understanding of the compaction rate and a better distribution of the shear stress changes, as well as an improved multiple-well configuration, which is better suited to a large-scale production field.

At the moment, our model does not account for a friction healing phase. Consequently, once the shear stress has dropped to its residual value (described by the dynamic coefficient of friction), it cannot be recovered. Hence, the simulation of multiple events on the same fault zone is limited. Our model is therefore appropriate for the processes happening before and during the first rupture but fails to explain the physics after the first reactivation. This could be important given that multiple ruptures on the same fault plane are indeed possible in an actual gas reservoir.

Another approximation is the use of the quasi-static approach, although our findings in terms of average slip and magnitude are firmly in agreement with the recent dynamic modeling results of production-induced seismicity [*Wassing et al*., 2016].

Finally, our model was designed to provide insights into the physics of production-induced seismicity by highlighting the most important factors that possibly lead to fault reactivation, particularly in a compartmentalized reservoir. Consequently, the model proposed here is largely deterministic with a known location for the fault plane. In a real case, a reservoir consists of numerous known and even more unknown faults crisscrossing the production reservoir. A deterministic model would hardly reproduce real data such as the distribution of seismic events and an earthquake's statistical analysis. A stochastic and statistical model would be better suited to a more substantive comparison to field observations. However, the deterministic model can be extrapolated to the case of a population of faults and compartments with different conditions in terms of stress and orientation. The entire population of faults would somehow behave similarly, but critical conditions can be reached before or later with respect to the case shown here. Hence, the evolution of the shear stress can be easily interpreted as related to an accelerating seismicity: the longer the production, the greater the shear stress will be, and the greater the possibility of inducing an earthquake. In terms of a prevention/mitigation strategy, extrapolating again to a diverse population of faults, on the one hand, our model would predict that a complete shut-in of gas production would lead to an average decrease in seismicity, although seismicity may still occur at some location even decades after shut-in. On the other hand, the injection of fluid is an effective mitigation strategy only when the production wells are sparse and not producing from a neighboring compartment.

Acknowledgments
This work was supported by a Swiss National Science Foundation (SNSF)—Ambizione Energy grant (PZENP2_160555). Technical review comments by Jonny Rutqvist (LBNL) greatly helped to improve the manuscript. We also would like to thank two anonymous reviewers for their thorough reviews and very useful comments. Data used as model input are referenced within this manuscript. Results of the numerical model are available by contacting the author at dominik.zbinden@sed.ethz.ch.

References

Bardainne, T., N. Dubos-Sallée, G. Sénéchal, P. Gaillot, and H. Perroud (2008), Analysis of the induced seismicity of the Lacq gas field (southwestern France) and model of deformation, *Geophys. J. Int.*, *172*(3), 1151–1162, doi:10.1111/j.1365-246X.2007.03705.x.

Biot, M. A. (1941), General theory of three-dimensional consolidation, *J. Appl. Phys.*, *12*(2), 155–164, doi:10.1063/1.1712886.

Cappa, F., and J. Rutqvist (2011a), Impact of CO_2 geological sequestration on the nucleation of earthquakes, *Geophys. Res. Lett.*, *38*, L17313, doi:10.1029/2011GL048487.

Cappa, F., and J. Rutqvist (2011b), Modeling of coupled deformation and permeability evolution during fault reactivation induced by deep underground injection of CO_2, *Int. J. Greenhouse Gas Control*, *5*(2), 336–346, doi:10.1016/j.ijggc.2010.08.005.

Cappa, F., and J. Rutqvist (2012), Seismic rupture and ground accelerations induced by CO_2 injection in the shallow crust, *Geophys. J. Int.*, *190*(3), 1784–1789, doi:10.1111/j.1365-246X.2012.05606.x.

Catalli, F., A. P. Rinaldi, V. Gischig, M. Nespoli, and S. Wiemer (2016), The importance of earthquake interactions for injection-induced seismicity: Retrospective modeling of the Basel enhanced geothermal system, *Geophys. Res. Lett.*, *43*, 4992–4999, doi:10.1002/2016GL068932.

Chang, K. W., and P. Segall (2016), Injection-induced seismicity on basement faults including poroelastic stressing, *J. Geophys. Res. Solid Earth*, *121*, 2708–2726, doi:10.1002/2015JB012561.

Corey, A. T. (1954), The interrelation between gas and oil relative permeabilities, *Prod. Mon.*, *19*(1), 38–41.

Committee on Induced Seismicity Potential in Energy Technologies (2013), *Induced Seismicity Potential in Energy Technologies*, 225 pp., Natl. Res. Counc., Washington, D. C. [Available at http://dels.nas.edu/Report/Induced-Seismicity-Potential-Energy-Technologies/13355.]

Dahm, T., S. Cesca, S. Hainzl, T. Braun, and F. Krüger (2015), Discrimination between induced, triggered, and natural earthquakes close to hydrocarbon reservoirs: A probabilistic approach based on the modeling of depletion-induced stress changes and seismological source parameters, *J. Geophys. Res. Solid Earth*, *120*, 2491–2509, doi:10.1002/2014JB011778.

Davies, J. P., and D. K. Davies (2001), Stress-dependent permeability: Characterization and modeling, *Soc. Pet. Eng. J.*, *6*, 224–235, doi:10.2118/71750-PA.

de Waal, J. A., A. G. Muntendam-Bos, and J. P. A. Roest (2015), Production induced subsidence and seismicity in the Groningen gas field—Can it be managed?, *Proc. Int. Assoc. Hydrol. Sci.*, *372*, 129–139, doi:10.5194/piahs-372-129-2015.

Ellsworth, W. L. (2013), Injection-induced earthquakes, *Science*, *341*(6142), doi:10.1126/science.1225942.

Ellsworth, W. L., A. L. Llenos, A. F. McGarr, A. J. Michael, J. L. Rubinstein, C. S. Mueller, M. D. Petersen, and E. Calais (2015), Increasing seismicity in the U.S. midcontinent: Implications for earthquake hazard, *Leading Edge*, *34*(6), 618–626, doi:10.1190/tle34060618.1.

Gercek, H. (2007), Poisson's ratio values for rocks, *Int. J. Rock Mech. Min. Sci.*, *44*(1), 1–13, doi:10.1016/j.ijrmms.2006.04.011.
Gischig, V., and S. Wiemer (2013), A stochastic model for induced seismicity based on non-linear pressure diffusion and irreversible permeability enhancement, *Geophys. J. Int.*, *194*(2), 1229–1249, doi:10.1093/gji/ggt164.
Goertz-Allmann, B. P., and S. Wiemer (2013), Geomechanical modeling of induced seismicity source parameters and implications for seismic hazard assessment, *Geophysics*, *78*(1), KS25–KS39, doi:10.1190/GEO2012-0102.1.
Grasso, J. R. (1992), Mechanics of seismic instabilities induced by the recovery of hydrocarbons, *Pure Appl. Geophys.*, *139*(3), 507–534, doi:10.1007/BF00879949.
Grasso, J. R., and G. Wittlinger (1990), Ten years of seismic monitoring over a gas field, *Bull. Seismol. Soc. Am.*, *80*(2), 450–473.
Grigoli, F., S. Cesca, E. Priolo, A. P. Rinaldi, J. F. Clinton, T. A. Stabile, B. Dost, M. Garcia Fernandez, S. Wiemer, and T. Dahm (2017), Current challenges in monitoring, discrimination and management of induced seismicity related to underground industrial activities: A European perspective, *Rev. Geophys.*, *55*, doi:10.1002/2016RG000542.
Hangx, S. J. T., C. J. Spiers, and C. J. Peach (2010), Mechanical behavior of anhydrite caprock and implications for CO_2 sealing capacity, *J. Geophys. Res.*, *115*, B07402, doi:10.1029/2009JB006954.
Herber, R., and J. De Jager (2010), Geoperspective oil and gas in the Netherlands—Is there a future?, *Neth. J. Geosci.*, *89*(2), 91–107.
Hettema, M. H. H., P. M. T. M. Schutjens, B. J. M. Verboom, and H. J. Gussinklo (2000), Production-induced compaction of a sandstone reservoir: The strong influence of stress path, *SPE Reserv. Eval. Eng.*, *3*(4), 342–347, doi:10.2118/65410-PA.
Hettema, M., E. Papamichos, and P. Schutjens (2002), Subsidence delay: Field observations and analysis, *Oil Gas Sci. Technol.*, *57*(5), 443–458, doi:10.2516/ogst:2002029.
ITASCA (2013) *FLAC3d v5.01, Fast Lagrangian Analysis of Continua in 3 Dimensions, User's Guide*, Itasca Consulting Group, Minneapolis, Minn.
Jeanne, P., Y. Guglielmi, F. Cappa, A. P. Rinaldi, and J. Rutqvist (2014), The effects of lateral property variations on fault-zone reactivation by fluid pressurization: Application to CO_2 pressurization effects within major and undetected fault zones, *J. Struct. Geol.*, *62*, 97–108, doi:10.1016/j.jsg.2014.01.017.
Jeanne, P., J. Rutqvist, A. P. Rinaldi, P. F. Dobson, M. Walters, C. Hartline, and J. Garcia (2015), Seismic and aseismic deformations and impact on reservoir permeability: The case of EGS stimulation at the Geysers, California, USA, *J. Geophys. Res. Solid Earth*, *120*, 7863–7882, doi:10.1002/2015JB012142.
Juanes, R., B. Jha, B. H. Hager, J. H. Shaw, A. Plesch, L. Astiz, J. H. Dieterich, and C. Frohlich (2016), Were the May 2012 Emilia-Romagna earthquakes induced? A coupled flow-geomechanics modeling assessment, *Geophys. Res. Lett.*, *43*, 6891–6897, doi:10.1002/2016GL069284.
Kanamori, H., and D. L. Anderson (1975), Theoretical basis of some empirical relations in seismology, *Bull. Seismol. Soc. Am.*, *65*(5), 1073–1095.
Kanamori, H., and E. E. Brodsky (2004), The physics of earthquakes, *Rep. Prog. Phys.*, *67*(8), 1429–1496, doi:10.1088/0034-4885/67/8/R03.
Mazzoldi, A., A. P. Rinaldi, A. Borgia, and J. Rutqvist (2012), Induced seismicity within geological carbon sequestration projects: Maximum earthquake magnitude and leakage potential from undetected faults, *Int. J. Greenhouse Gas Control*, *10*, 434–442, doi:10.1016/j.ijggc.2012.07.012.
McGarr, A., D. Simpson, and L. Seeber (2002), 40 case histories of induced and triggered seismicity, *Int. Geophys.*, *81A*, 647–661.
Mulders, F. M. M. (2003), Modelling of stress development and fault slip in and around a producing gas reservoir, PhD thesis, Tech. Univ. of Delft.
NAM (2013), Technical addendum to the Winningsplan Groningen 2013: Subsidence induced earthquakes and seismic hazard analysis in the Groningen field, November 2013.
Nasrifar, K., and O. Bolland (2006), Prediction of thermodynamic properties of natural gas mixtures using 10 equations of state including a new cubic two-constant equation of state, *J. Pet. Sci. Eng.*, *51*(3), 253–266, doi:10.1016/j.petrol.2006.01.004.
Orlic, B. (2016), Geomechanical effects of CO_2 storage in depleted gas reservoirs in the Netherlands: Inferences from feasibility studies and comparison with aquifer storage, *J. Rock Mech. Geotech. Eng.*, *8*, 846–859, doi:10.1016/j.jrmge.2016.07.003.
Orlic, B., Wassing, B. B. T., and Geel, C. R. (2013), Field scale geomechanical modeling for prediction of fault stability during underground gas storage operations in a depleted gas field in the Netherlands, Proceedings of the 47th US Rock Mechanics/Geomechanics Symposium, San Francisco, 23–26 June.
Pruess, K., Oldenburg, C. M., and Moridis, G. (2011), TOUGH2 User's Guide, Version 2.1, Paper LBNL-43134 (revised), Lawrence Berkeley Natl. Lab., Berkeley, Calif.
Rahimpour-Bonab, H., B. Esrafili-Dizaji, and V. Tavakoli (2010), Dolomitization and anhydrite precipitation in Permo-Triassic carbonates at the South Pars Gasfield, offshore Iran: Controls on reservoir quality, *J. Pet. Geol.*, *33*(1), 43–66.
Rinaldi, A. P., and M. Nespoli (2017), TOUGH2-SEED: A coupled fluid flow and mechanical-stochastic approach to model injection-induced seismicity, *Comput. Geosci.*, doi:10.1016/j.cageo.2016.12.003.
Rinaldi, A. P., and J. Rutqvist (2013), Modeling of deep fracture zone opening and transient ground surface uplift at KB-502 CO_2 injection well, In Salah, Algeria, *Int. J. Greenhouse Gas Control*, *12*, 155–167, doi:10.1016/j.ijggc.2012.10.017.
Rinaldi, A. P., P. Jeanne, J. Rutqvist, F. Cappa, and Y. Guglielmi (2014a), Effects of fault-zone architecture on earthquake magnitude and gas leakage related to CO_2 injection in a multi-layered sedimentary system, *Greenhouse Gases: Sci. Technol.*, *4*, 99–120, doi:10.1002/ghg.1403.
Rinaldi, A. P., J. Rutqvist, and F. Cappa (2014b), Geomechanical effects on CO_2 leakage through fault zones during large-scale underground injection, *Int. J. Greenhouse Gas Control*, *20*, 171–131, doi:10.1016/j.ijggc.2013.11.001.
Rinaldi, A. P., Vilarrasa, V., Rutqvist, J., and Cappa, F. (2014c), 3D modeling of fault reactivation during CO_2 injection, Abstract H11K-05 presented at 2014, Fall Meeting, AGU, San Francisco, Calif., 15–19 Dec.
Rinaldi, A. P., J. Rutqvist, E. Sonnenthal, and T. T. Cladouhos (2015a), Coupled THM modeling of hydroshearing stimulation in tight fractured volcanic rock, *Tranport Porous Media*, *108*(1), 131–150, doi:10.1007/s11242-014-0296-5.
Rinaldi, A. P., V. Vilarrasa, J. Rutqvist, and F. Cappa (2015b), Fault reactivation during CO_2 sequestration: Effects of well orientation on seismicity and leakage, *Greenhouse Gases: Sci. Technol.*, *5*, 645–656, doi:10.1002/ghg.1511.
Rinaldi, A. P., J. Rutqvist, S. Finsterle, and H. H. Liu (2017), Inverse modeling of ground surface uplift and pressure with iTOUGH-PEST and TOUGH-FLAC: The case of CO_2 injection at In Salah, Algeria, *Comput. Geosci.*, doi:10.1016/j.cageo.2016.10.009.
Rutqvist, J. (2011), Status of the TOUGH-FLAC simulator and recent applications related to coupled fluid flow and crustal deformations, *Comput. Geosci.*, *37*(6), 739–750, doi:10.1016/j.cageo.2010.08.006.
Rutqvist, J., and O. Stephansson (2003), The role of hydromechanical coupling in fractured rock engineering, *Hydrogeol. J.*, *11*(1), 7–40, doi:10.1007/s10040-002-0241-5.
Rutqvist, J., and C. F. Tsang (2002), A study of caprock hydromechanical changes associated with CO_2-injection into a brine formation, *Environ. Geol.*, *42*(2–3), 296–305, doi:10.1007/s00254-001-0499-2.
Rutqvist, J., Y.-S. Wu, C.-F. Tsang, and G. Bodvarsson (2002), A modeling approach for analysis of coupled multiphase fluid flow, heat transfer, and deformation in fractured porous rock, *Int. J. Rock Mech. Min. Sci.*, *39*(4), 429–442, doi:10.1016/S1365-1609(02)00022-9.

Rutqvist, J., G. J. Moridis, T. Grover, and T. Collett (2009), Geomechanical response of permafrost-associated hydrate deposits to depressurization-induced gas production, *J. Pet. Sci. Eng.*, *67*, 1–12.

Rutqvist, J., G. J. Moridis, T. Grover, S. Silpngarmlert, T. S. Collett, and S. A. Holdich (2012), Coupled multiphase fluid flow and wellbore stability analysis associated with gas production from oceanic hydrate-bearing sediments, *J. Pet. Sci. Eng.*, *92–93*, 65–81, doi:10.1029/2012RG000391.

Rutqvist, J., P. F. Dobson, J. Garcia, C. Hartline, P. Jeanne, C. M. Oldenburg, D. W. Vasco, and M. Walters (2013a), The Northwest Geysers EGS Demonstration Project, California: Pre-stimulation modeling and interpretation of the stimulation, *Math. Geosci.*, *47*(1), 3–29, doi:10.1007/s11004-013-9493-y.

Rutqvist, J., A. P. Rinaldi, F. Cappa, and G. J. Moridis (2013b), Modeling of fault reactivation and induced seismicity during hydraulic fracturing of shale-gas reservoirs, *J. Pet. Sci. Eng.*, *107*, 31–44, doi:10.1016/j.petrol.2013.04.023.

Rutqvist, J., F. Cappa, A. P. Rinaldi, and M. Godano (2014), Modeling of induced seismicity and ground vibrations associated with geological CO_2 storage, and assessing their effects on surface structures and human perception, *Int. J. Greenhouse Gas Control*, *24*, 64–77, doi:10.1016/j.ijggc.2014.02.017.

Rutqvist, J., A. P. Rinaldi, F. Cappa, and G. J. Moridis (2015), Modeling of fault activation and seismicity by injection directly into a fault zone associated with hydraulic fracturing of shale-gas reservoirs, *J. Pet. Sci. Eng.*, *127*, 377–386, doi:10.1016/j.petrol.2015.01.019.

Rutqvist, J., A. P. Rinaldi, F. Cappa, P. Jeanne, A. Mazzoldi, L. Urpi, Y. Guglielmi, and V. Vilarrasa (2016), Fault activation and induced seismicity in geologic carbon storage—Lessons learned from recent modeling studies, *J. Rock Mech. Geotech. Eng.*, *8*, 789–804, doi:10.1016/j.jrmge.2016.09.001.

Sanz, P. F., S. P. Lele, K. H. Searles, S.-Y. Hsu, J. L. Garzon, J. A. Burdette, W. E. Kline, B. A. Dale, and P. D. Hector (2015), Geomechanical analysis to evaluate production-induced fault reactivation at Groningen gas field, SPE Annual Technical Conference and Exhibition, doi:10.2118/174942-MS.

Schutjens, P. M. T. M., Hanssen, T. H., Hettema, M. H. H., Merour, J., J. P. de Bree, Coremans, J. W. A., and Helliesen, G. (2001), Compaction-induced porosity/permeability reduction in sandstone reservoirs, SPE Annual Technical Conference and Exhibition, doi:10.2118/71337-ms.

Segall, P. (1989), Earthquakes triggered by fluid extraction, *Geology*, *17*, 942–946, doi:10.1130/0091-7613(1989)017<0942:ETBFE>2.3.CO;2.

Segall, P., J. R. Grasso, and A. Mossop (1994), Poroelastic stressing and induced seismicity near the Lacq gas field, southwestern France, *J. Geophys. Res.*, *99*(B8), 15,423–15,438, doi:10.1029/94JB00989.

Segall, P., and S. D. Fitzgerald (1998), A note on induced stress changes in hydrocarbon and geothermal reservoirs, *Tectonophysics*, *289*(1), 117–128, doi:10.1016/S0040-1951(97)00311-9.

Shapiro, S. A., and C. Dinske (2009), Scaling of seismicity induced by non-linear fluid–rock interaction, *J. Geophys. Res.*, *114*, B09307, doi:10.1029/2008JB006145.

Styles, P., P. Gasparini, E. Huenges, P. Scandone, S. Lasocki, and F. Terlizzese (2014), Report on the hydrocarbon exploration and seismicity in Emilia region, International Commission on Hydrocarbon Exploration and Seismicity in the Emilia Region (ICHESE) February, pp. 1–213.

Terzaghi, K. V. (1923), Die Berechnung der Durchlässigkeitsziffer des Tones aus dem Verlauf der hydrodynamischen Spannungserscheinungen, *Sitzungsber. Akad. Wiss. Wien, Math.-Naturwiss. Kl., Abt. 2A*, *132*, 125–138.

Trutnevyte, E., and S. Wiemer (2017), Tailor-made risk governance for induced seismicity of geothermal energy projects: An application to Switzerland, *Geothermics*, *65*, 295–312, doi:10.1016/j.geothermics.2016.10.006.

TNO (2012), Deterministische hazard analyse voor geinduceerde seismiciteit in Nederland, TNO rapport 2012 R10198, 25 June 2012.

TNO (2013), Toesting van de bodemdalingsprognoses en seismiche hazard ten gevolve van gaswinning van het Groningen veld, TNO rapport 2013 R11953, 23 December 2013.

Urpi, L., A. P. Rinaldi, J. Rutqvist, F. Cappa, and C. J. Spiers (2016), Dynamic simulation of CO_2-injection-induced fault rupture with slip-rate dependent friction coefficient, *Geomech. Energy Environ.*, *7*, 47–65, doi:10.1016/j.gete.2016.04.003.

van den Bogert, P. A. J. (2015), Impact of various modelling options on the onset of fault slip and fault slip response using 2-dimensional finite-element modelling, Restricted report No. SR.15.11455, Shell Global Solutions International B.V, Rijswijk.

van Genuchten, M. T. (1980), A closed-form equation for predicting the hydraulic conductivity of unsaturated soils, *Soil Sci. Soc. Am. J.*, *44*(5), 892–898.

Van Hulten, F. F. N. (2010), Geological factors effecting compartmentalization of Rotliegend gas fields in the Netherlands, *Geol. Soc.*, *347*(1), 301–315, doi:10.1144/SP347.17.

van Thienen-Visser, K., and J. N. Breunese (2015), Induced seismicity of the Groningen gas field, *Leading Edge*, *34*(6), 664–671, doi:10.1190/tle34060664.1.

Van Wees, J. D., L. Buijze, K. Van Thienen-Visser, M. Nepveu, B. B. T. Wassing, B. Orlic, and P. A. Fokker (2014), Geomechanics response and induced seismicity during gas field depletion in the Netherlands, *Geothermics*, *52*, 206–219, doi:10.1016/j.geothermics.2014.05.004.

Wassing, B. B. T., L. Buijze, and B. Orlic (2016), Modelling of fault reactivation and fault slip in producing gas fields using a slip-weakening friction law, in *Proceedings of 50th US Rock Mechanics/Geomechanics Symposium*, ARMA 16-658, 11 p., Houston, Tex.

Zoback, M. D. (2010) *Reservoir Geomechanics*, pp. 402–408, Cambridge Univ. Press, New York.